nature communications



Article

https://doi.org/10.1038/s41467-025-56342-7

Nonapoptotic caspase-3 guides C1qdependent synaptic phagocytosis by microglia

Received: 20 November 2023

Accepted: 15 January 2025

Published online: 22 January 2025

Check for updates

Megumi Andoh^{1,2}, Natsuki Shinoda^{3,7}, Yusuke Taira^{3,7}, Tasuku Araki [®] ², Yuka Kasahara², Haruki Takeuchi⁴, Masayuki Miura [®] ³, Yuji Ikegaya [®] ^{2,5,6} & Ryuta Koyama [®] ^{1,2,5} ⊠

Caspases are known to mediate neuronal apoptosis during brain development. However, here we show that nonapoptotic activation of caspase-3 at presynapses drives microglial synaptic phagocytosis. Real-time observation and spatiotemporal manipulation of synaptic caspase-3 in the newly established, mouse-derived culture system demonstrate that increased neuronal activity triggers localized presynaptic caspase-3 activation, facilitating synaptic tagging by complements. High-resolution live imaging reveals that caspase-3 activation promotes synapse-selective complement-dependent microglial phagocytosis without axonal shearing. Furthermore, activity-dependent caspase-3 activation at inhibitory presynapses induces microglial phagocytosis in mice and increases seizure susceptibility. This increased susceptibility is reversed by genetic depletion of microglial complement receptors. Thus, localized, nonapoptotic caspase activity guides complement-dependent microglial synaptic phagocytosis and remodels neuronal circuits.

Caspase-3 is a central effector of neuronal apoptosis in the central nervous system, playing a critical role in brain development. During early development, caspase-3-mediated apoptosis shapes neuronal circuits by eliminating excess neurons, thereby ensuring proper brain patterning^{1,2}. However, studies focusing on postnatal and adult neuroplasticity have identified a distinct, nonapoptotic role for caspase-3: localized activation of caspase-3 influences neuronal morphology and function by mediating dendritic and axonal pruning as well as regulating synaptic plasticity^{3–7}.

Nonapoptotic caspase-3 activation has been observed in dendritic spines, where it influences long-term depression (LTD) and synaptic shrinkage, processes critical for learning and memory⁵⁻⁸. Spatial and temporal regulation of nonapoptotic caspases-3 allows for synaptic modifications without inducing cell death. Despite these insights, the

involvement of caspase-3 in glial cell-mediated synaptic pruning remains largely unexplored.

Microglia, the resident macrophages of the brain parenchyma, play a key role in synaptic pruning, which is essential for neuronal circuit maturation and plasticity^{9,10}. Microglial synaptic pruning is primarily mediated by the classical complement cascade, initiated by the binding of complement protein C1q to synapses⁹. Notably, synaptosome analysis suggests the colocalization of C1q with activated caspase-3 at presynapses¹¹, raising the possibility that presynaptic caspase-3 activation triggers C1q tagging and subsequent microglial phagocytosis. However, the mechanisms linking presynaptic caspase-3 activation to complement-mediated microglial pruning remain unclear. Key questions include how presynaptic caspase-3 activation is triggered, its spatiotemporal relationship with C1q tagging, and

¹Department of Translational Neurobiology, National Institute of Neuroscience, National Center of Neurology and Psychiatry, Kodaira, Tokyo 187-8502, Japan. ²Laboratory of Chemical Pharmacology, Graduate School of Pharmaceutical Sciences, The University of Tokyo, Bunkyo-ku, Tokyo 113-0033, Japan. ³Department of Genetics, Graduate School of Pharmaceutical Sciences, The University of Tokyo, Bunkyo-ku, Tokyo 113-0033, Japan. ⁴Laboratory of Molecular Neurobiology, Department of Biophysics and Biochemistry, The University of Tokyo, Bunkyo-ku, Tokyo 113-0032, Japan. ⁵Institute for AI and Beyond, The University of Tokyo, Bunkyo-ku, National Institute of Information and Communications Technology, Suita City, Osaka 565-0871, Japan. ⁷These authors contributed equally: Natsuki Shinoda, Yusuke Taira. whether this activation selectively drives microglial phagocytosis of presynapses.

In this study, we aimed to address these knowledge gaps by investigating the role of nonapoptotic caspase-3 activation in synaptic pruning and circuit remodeling. Using high-resolution live imaging and innovative tools to manipulate and detect synaptic caspase-3 activity in vitro, we investigated the relationship between caspase-3 activation, synaptic tagging by complement, and microglial phagocytosis. Additionally, we employed an in vivo febrile seizure (FS) model to validate the impact of caspase-3-driven synaptic phagocytosis on neuronal circuit remodeling and function.

We found that nonapoptotic caspase-3 activation at presynaptic sites facilitates complement-dependent microglial phagocytosis under elevated neuronal activity. These findings reveal an activity-dependent mechanism of synaptic refinement with implications for both normal brain function and neurodevelopmental or neurodegenerative disorders. Specifically, the pruning of highly active synapses may contribute to maintaining synaptic network homeostasis beyond pathological conditions characterized by abnormal pruning.

Results

Increased neuronal activity triggers localized caspase-3 activation at presynapses

To investigate synaptic caspase-3 activation at high resolution in real time, we first cocultured neurons and microglia with astrocytes to mimic the ramified morphology of microglia, which might be essential for synaptic phagocytosis¹² (Supplementary Fig. 1a, b; Supplementary Movie 1). RT-qPCR analysis confirmed that microglia in the coculture express microglia-related genes, including homeostatic genes but not monocyte-related genes (Supplementary Fig. 1c). We also confirmed that excitatory and inhibitory synaptogenesis occurred over time (Supplementary Fig. 1d–g) and that both excitatory and inhibitory presynapses were phagocytosed by microglia (Supplementary Fig. 1hk) in our coculture system. For live imaging, we labeled these presvnapses with adeno-associated virus (AAV) synaptophysin-mCherry under the hSyn promoter (Supplementary Fig. 1l, m).

Increased neuronal activity opens voltage-gated calcium channels (VGCCs), leading to an influx of calcium ions¹³. When calcium ion influx into mitochondria becomes excessive, caspase-3 is activated through cytochrome c release into the cytosol¹⁴. Since increased neuronal activity leads to mitochondrial accumulation at presynapses¹⁵, it is conceivable that caspase-3 is activated at these locations. To explore this hypothesis, we employed an AAV to introduce hM3Dq, a designer receptor exclusively activated by designer drugs (DREADD), into neurons using the hSyn promoter. hM3Dq specifically responds to the artificial ligand clozapine-N-oxide (CNO), inducing calcium ion influx and neuronal firing. CNO application increased neuronal activity and the abundance of presynaptic mitochondria in hM3Dq-expressing neurons, a result corroborated by c-Fos immunostaining and live mitochondrial imaging (Supplementary Fig. 2). Subsequent immunostaining revealed localized cleaved caspase-3, a marker for activated caspase-3, at presynapses labeled with synaptophysin-mCherry; cleaved caspase-3 signals were significantly increased in the CNO group (Fig. 1a, b). This hM3Dq-driven increase was blocked by the caspase-3 inhibitor Z-DEVD-FMK (10 µM) (Fig. 1b). Compared to the presynapses, the neuronal soma and axonal shafts showed lower cleaved caspase-3 signals, suggesting nonapoptotic caspase-3 activation (Fig. 1c, d).

To monitor caspase-3 activation in real time, we developed a new probe named the monomeric sensor for activated caspase based on fluorescence resonance energy transfer (FRET), or mSCAT3 (Fig. 1e; Supplementary Fig. 3a–c). In its steady state, mSCAT3 allows FRET between mECFP and mVenus, thereby decreasing the mECFP/mVenus ratio. Upon caspase-3 activation, the DEVD sequence linking mECFP

and mVenus is cleaved, leading to an increased mECFP/mVenus ratio (Fig. 1e: Supplementary Fig. 3b, c). We fused mSCAT3 to synaptophysin (synaptophysin-mSCAT3) for specific observation at presynapses. Although conventional SCAT3 tends to aggregate when fused with synaptophysin, we addressed this issue by introducing a monomeric mutation to SCAT3 (Supplementary Fig. 3a). mSCAT3 and synaptophsin-mSCAT3 were able to monitor DEVDase activity in response to apoptotic stimulation by TNF α and cycloheximide (CHX). The time course of caspase activation detection during apoptosis using these probes was identical to that of SCAT3 (Supplementary Fig. 3b)¹⁶. Thus, these probes were found to detect caspase activity with high sensitivity. To relate the mECFP/mVenus ratio of synaptophysin-mSCAT3 to actual caspase-3 activation, we measured FRET in live neurons, followed by immunostaining for cleaved caspase-3 (Fig. 1f, g). We analyzed the maximum mECFP/mVenus ratio at each presynapse based on the presence or absence of cleaved caspase-3 signals. The distribution of the maximum mECFP/mVenus ratio showed a clear division between cleaved caspase-3-negative and -positive presynapses (Fig. 1g). We inferred caspase-3 activation when the mECFP/mVenus ratio was 1 or higher, as the mean mode of the mECFP/mVenus ratio of cleaved caspase-3-negative presynapses and that of cleaved caspase-3-positive presynapses was 1. Consequently, live imaging of hM3Dq-expressing neurons after CNO application showed an increased mECFP/mVenus ratio at specific presynapses, a pattern not seen with dimethylsulfoxide (DMSO) application (Fig. 1h, j). There was a significant increase in the proportion of presynapses with a ratio of 1 or higher after CNO application (Fig. 1i, k). In addition, we confirmed the specificity of synaptophysin-mSCAT3 response in the neuron-glia cocultures by showing that CNO application did not increase the proportion of presynapses with a ratio of 1 or higher in neurons expressing synaptophysin-mSCAT3^{DEVG}, a negative control for synaptophysin-mSCAT3 (CNO Pre: 2.137%; CNO 6 h: 1.46%, median, n=11 regions each from two independent experiments, P > 0.05, Wilcoxon signed-rank test).

We further investigated the involvement of mitochondrial cytochrome c release in presynaptic caspase-3 activation because of the link between activity-dependent Ca2+ influx, mitochondrial cytochrome c release, and caspase-3 activation¹³⁻¹⁵. To suppress cytochrome c release and subsequent caspase-9 activation, we used Bax channel blocker (2 µM) and NS3694 (Apaf-1 inhibitor, 2 µM), respectively. As a result, while CNO application significantly increased the proportion of presynapses with increased caspase-3 activity, this increase was inhibited in the CNO + Bax channel blocker and CNO + NS3694 groups (Supplementary Fig. 3d). We further assessed the correlation between mitochondrial accumulation and caspase activity at presynapses using live imaging of mito-DsRed and synaptophysinmSCAT3, which suggested a positive correlation between them (Supplementary Fig. 4). These results suggest that increased neuronal activity may trigger presynaptic caspase-3 activation through mitochondrial accumulation, cytochrome c release, and subsequent caspase-9 activation.

It should be noted that the above results did not reflect any offtarget effects of CNO, as CNO application did not affect synaptic distribution (Supplementary Fig. 5) or presynaptic caspase-3 activation (Supplementary Fig. 3d) in neurons that did not express hM3Dq.

Presynaptic caspase-3 activation amplifies complementdependent microglial synaptic phagocytosis

Previous synaptosome analyses have shown that C1q is more prone to colocalize with synaptosomes containing cleaved caspase-3¹¹. It has been established that synaptic tagging by C1q, which triggers the complement cascade and C3 tagging of synapses, induces microglial synaptic phagocytosis through the activation of microglial complement receptor 3 (CR3) under both physiological and pathological conditions^{9,17-20}. These findings imply that presynaptic caspase-3

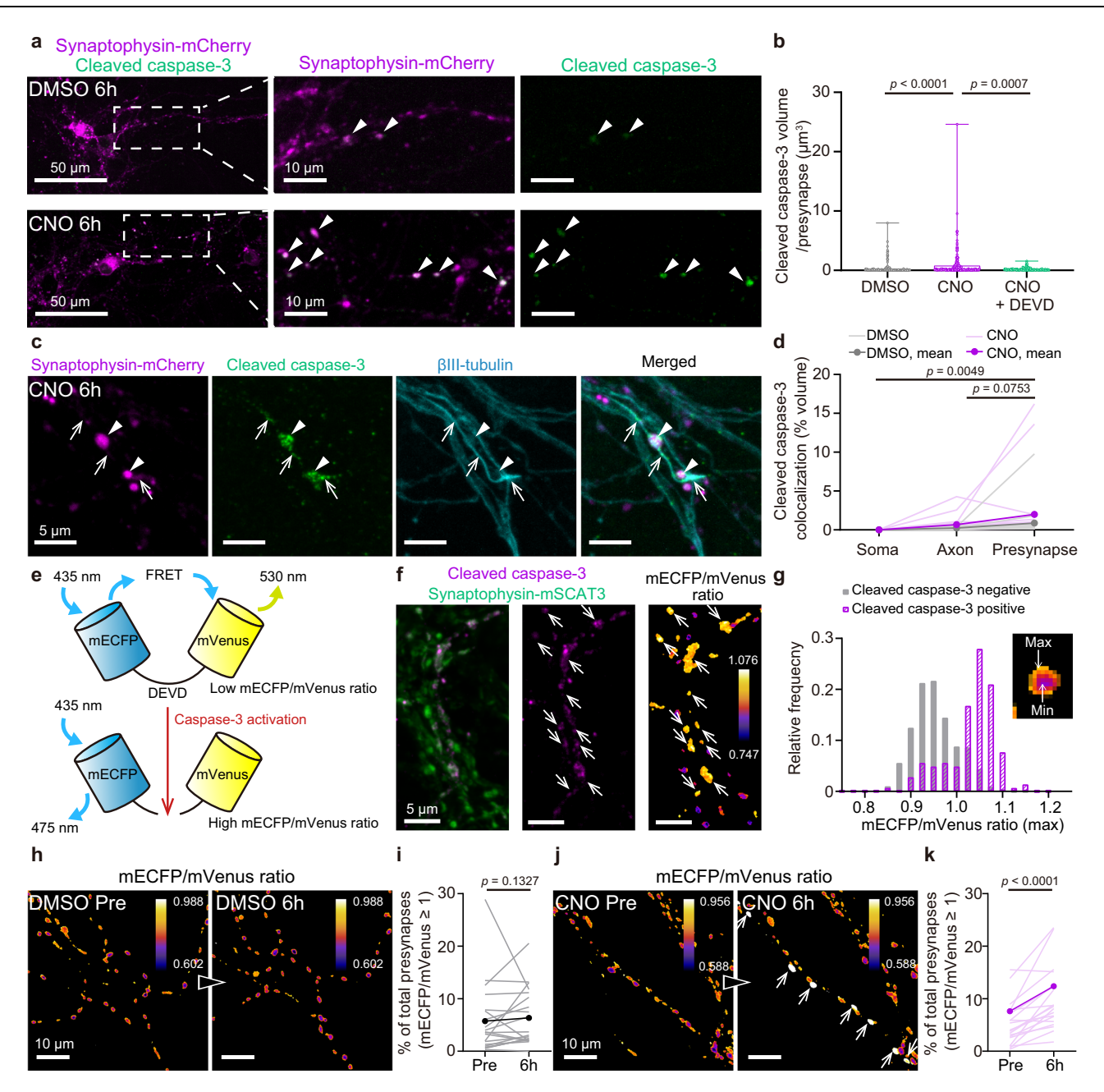
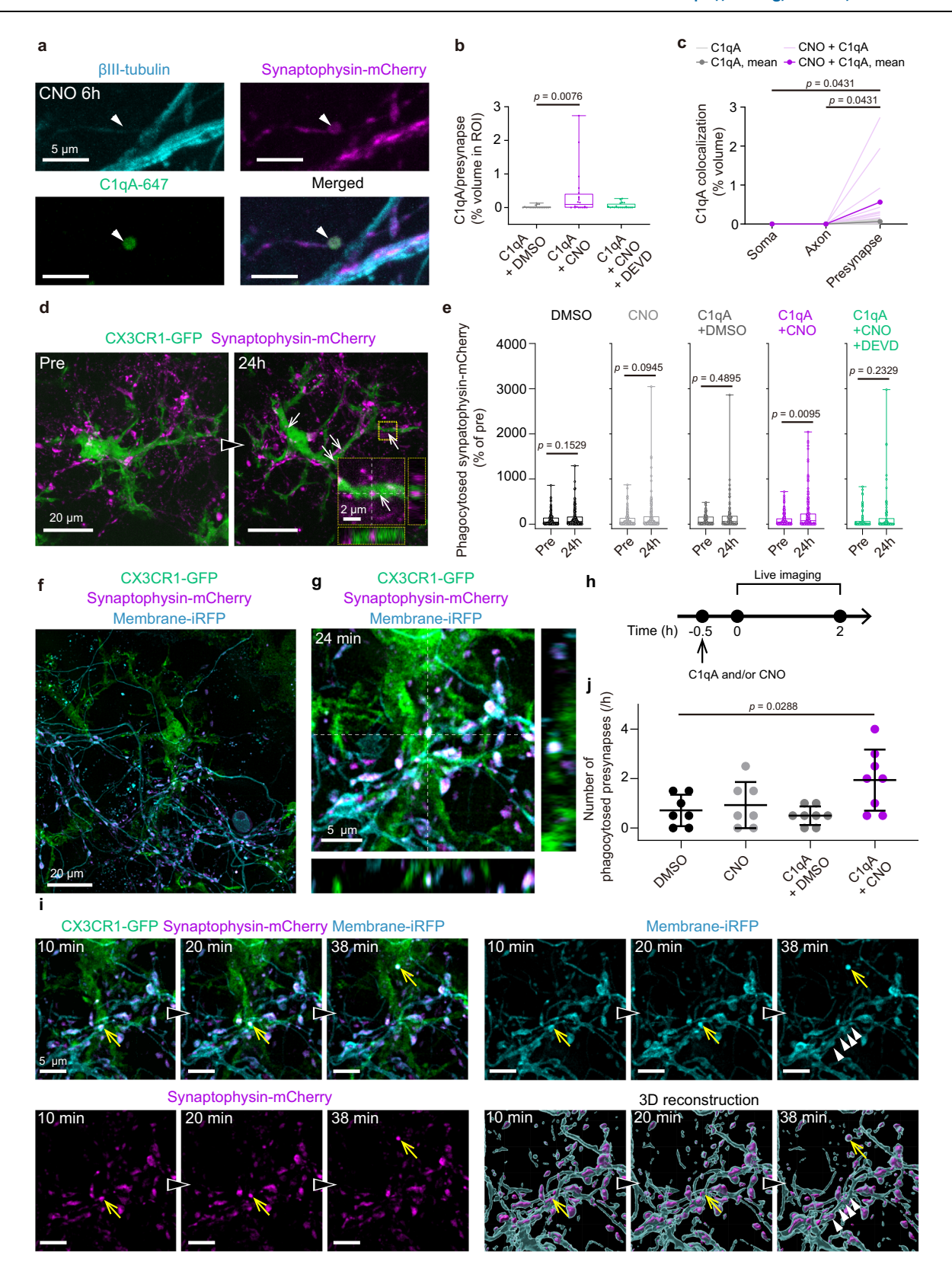


Fig. 1 | Increased neuronal activity triggers local caspase-3 activation at presynapses. a Representative images of cultured neurons expressing synaptophysinmCherry (left) 6 hours after drug application. The middle and right panels are magnified images of the dashed-line square in the left panel. Arrowheads indicate caspase-3 immunosignals in presynapses. **b** Cleaved caspase-3 volume in a presynaptic bouton 6 hours after drug application. DEVD refers to the caspase-3 inhibitor Z-DEVD-FMK. Mean \pm SD, n = 121, 188, 124 presynapses in 20 regions from 2 independent experiments, Dunn's test after one-way ANOVA on ranks. Box plots are defined as follows: the central line within the box represents the median (50th percentile), while the bounds of the box represent the 25th and 75th percentiles. The whiskers extend to the minimum and maximum values. All individual data points are plotted. c Representative images of cleaved caspase-3 in presynapses (arrowheads) and BIII-tubulin-immunostained axons (arrows) 6 hours after drug application. d Cleaved caspase-3 signals in H2B-GFP-positive soma, βIII-tubulinimmunostained axons and synaptophysin-mCherry-positive presynapses 6 hours after drug application. Plots from the same region are connected with a line. n = 20

regions from 2 independent experiments, Tukey's test after two-way repeatedmeasures ANOVA. e Diagram illustrating the real-time caspase-3 activity assay using mSCAT3. f Images displaying cleaved caspase-3 detected by immunocytochemistry (left, center) and the mECFP/mVenus ratio for synaptophysin-mSCAT3 (right). Arrows indicate cleaved caspase-3-positive presynapses. The experiment was independently repeated 2 times with similar results. g Frequency distribution of maximum mECFP/mVenus ratios in presynapses, based on the presence (magenta bars) or absence (gray bars) of cleaved caspase-3 signals. The inset image shows the mECFP/mVenus ratio in a single presynapse, and arrows point to the maximum and minimum ratios. n = 143 (cleaved caspase-3 positive), 1576 (cleaved caspase-3 negative) presynapses in 3 regions from 2 independent experiments. h, j Images showing the mECFP/mVenus ratio for synaptophysin-mSCAT3 before and after drug application. Arrows indicate presynapses whose mECFP/mVenus ratio is 1 or higher. i, k Proportion of presynapses whose mECFP/mVenus ratio is 1 or higher. n = 20 regions from 3 independent experiments, two-sided Wilcoxon signed-rank test (i), two-sided paired t test (k). Source data are provided as a Source Data file.



activation could drive complement-dependent synaptic phagocytosis by microglia.

To investigate the impact of hM3Dq-induced caspase-3 activation on synaptic tagging by C1q, we activated neuronal hM3Dq and applied fluorescently labeled mouse recombinant C1qA (C1qA-647), a major constituent of C1q, to cell cultures (Supplementary Fig. 6). We confirmed that C1qA-647-derived puncta were immunostained by both

anti-CIqA and anti-CIq antibodies, suggesting that CIqA-647 is integrated into CIq (Supplementary Fig. 6). Notably, the localization of CIqA-647 to presynapses significantly increased upon CNO application and was suppressed to control levels when the cells were cotreated with the caspase-3 inhibitor Z-DEVD-FMK (Fig. 2a, b). We also confirmed that CIqA-647 was preferentially localized to presynapses (Fig. 2c), similar to cleaved caspase-3 (Fig. 1d). These results suggest

Fig. 2 | Presynaptic caspase-3 activation promotes complement-dependent synaptic phagocytosis by microglia. a Images displaying colocalization between ClqA-647 and a presynaptic bouton (arrowheads) at 6 hours after CNO application. **b** Proportion of presynapses colocalized with ClqA-647 6 hours after drug application. DEVD refers to the caspase-3 inhibitor Z-DEVD-FMK. Mean \pm SD, n = 20regions from 2 independent experiments, Dunn's test after one-way ANOVA on ranks. Box plots are defined as follows: the central line within the box represents the median (50th percentile), while the bounds of the box represent the 25th and 75th percentiles. The whiskers extend to the minimum and maximum values. All individual data points are plotted. c C1qA-647 signals in H2B-GFP-positive soma, BIII-tubulin-immunostained axons and synaptophysin-mCherry-positive presynapses at 6 hours after drug application. Plots from the same region are connected with a line, n = 7.14 regions from 2 independent experiments. Tukev's test after two-way repeated-measures ANOVA. d Images displaying a time-lapse assay monitoring synaptic phagocytosis by microglia. Arrows indicate phagocytosed synaptophysin-mCherry. The inset image is an orthogonal view of the yellow-line square. e Volumetric assay of synaptophysin-mCherry signals within microglia before and after drug application. Mean \pm SD, DMSO: n = 170, 193 microglia from 4 independent experiments; CNO: n = 155, 172 microglia from 4 independent experiments; C1qA + DMSO: n = 92, 96 microglia from 3 independent experiments;

C1qA + CNO: n = 163, 173 microglia from 4 independent experiments; C1qA + CNO + DEVD: n = 79, 82 microglia from 3 independent experiments, two-sided Mann-Whitney U test. Box plots are defined as follows: the central line within the box represents the median (50th percentile), while the bounds of the box represent the 25th and 75th percentiles. The whiskers extend to the minimum and maximum values. All individual data points are plotted. f A representative image of microglia, presynapses, and axons in the coculture system. The experiment was independently repeated 30 times with similar results. g An orthogonal view showing the phagocytosis of a presynapse by microglia 24 minutes after starting live imaging. h Timeline showing drug application and live imaging of microglial synaptic phagocytosis. i Snapshots of live imaging representing microglial synaptic phagocytosis in control (DMSO) and corresponding 3D reconstructed images of presynapses and axons. Arrows indicate synaptophysin-mCherry-positive puncta phagocytosed by microglia. Arrowheads indicate the axon where phagocytosis occurred. The elapse time from the start of live imaging is shown in the upper left corner of each image. j Number of presynaptic puncta phagocytosed by microglia during the continuous 2-hour live imaging session. Mean \pm SD, n = 7 (DMSO), 7 (CNO), 8 (C1qA + DMSO), 8 (C1qA + CNO) independent experiments, Dunnett's test after one-way ANOVA. Source data are provided as a Source Data file.

that presynaptic caspase-3 activation promotes complement tagging. Some studies highlight the enhancement of phosphatidylserine (PS) externalization by caspase-3 activation²¹ and the subsequent binding of PS to C1q²². Here, we examined PS exposure using Annexin V conjugates. We confirmed that presynaptic PS exposure is promoted by increased neuronal activity and is reversed to control levels when caspase activity is inhibited by Z-DEVD-FMK (Supplementary Fig. 7). Thus, PS exposure in synaptic membrane is a potential mechanism to restrict C1q labeling to specific synapses.

Next, we investigated whether hM3Dq-induced caspase-3 activation boosts microglial synaptic phagocytosis. We conducted live imaging to compare the volume of presynapses phagocytosed by microglia derived from CX3CR1-GFP heterozygous mice, in which microglia were labeled with GFP, before and after drug application (Fig. 2d). We noted an enhancement in complement-dependent synaptic phagocytosis following hM3Dq activation, which was suppressed by the caspase-3 inhibitor Z-DEVD-FMK (Fig. 2e). This finding further reinforces the connection between hM3Dq-induced complement-dependent tagging and microglial phagocytosis through presynaptic caspase-3 activation.

To test whether presynaptic caspase-3 activation induces presynapse-specific phagocytosis by microglia, we conducted live imaging of synapse-microglia interactions following hM3Dq activation. Microglia, neuronal membranes, and presynaptic proteins were fluorescently labeled using CX3CR1-GFP mice or AAV-mediated transfection (Fig. 2f). We successfully documented ramified microglia engaging in presynaptic phagocytosis (Fig. 2g, i; Supplementary Movie 2, 3) and found that the axonal structure remained intact both before and after the phagocytic event (Fig. 2i; Supplementary Movie 4). This unprecedented observation reveals that microglia can selectively phagocytose presynapses without shearing axons. Furthermore, the phagocytosed synaptic proteins remained enveloped in the neuronal membrane (Fig. 2i). This synapse-selective phagocytosis significantly increased only when hM3Dq was activated in the presence of complement (Fig. 2h, j). We validated that the presynaptic area and microglial number in each region of interest (ROI) were comparable between groups (Supplementary Fig. 8). Importantly, we also confirmed that microglial synaptic phagocytosis (10, 13, 8, and 31 events in DMSO, CNO, C1qA + DMSO, and C1qA + CNO conditions, respectively) did not cause neuronal death, as the neuronal nuclei were intact during live imaging. We further confirmed that hM3Dq-induced increased activity did not induce neuronal death by performing TUNEL staining 6 hours after drug treatment. No neuronal death was observed (0%, 10 regions from 2 independent experiments).

A previous study suggested that the axon terminals from less active neurons are preferentially phagocytosed in the developing lateral geniculate nucleus. Here, we investigated whether decreased neuronal activity affects presynaptic caspase activation and synaptic phagocytosis by microglia using hM4Di, an inhibitory DREADD (Supplementary Fig. 9a, b). We confirmed that decreased activity does not significantly reduce synaptic caspase activity compared to the control group through live imaging of synaptophysin-mSCAT3 (Supplementary Fig. 9c, d). We also assessed synaptic phagocytosis by microglia and confirmed that it was decreased with inhibited neuronal activity (Supplementary Fig. 9e, f). From these results, we hypothesize that caspase-dependent synaptic phagocytosis is applied to highly active synapses to balance excitatory/inhibitory synapses during homeostatic circuit remodeling.

Presynaptic caspase-3 activation through optogenetics induces complement-dependent synaptic phagocytosis

To further clarify the role of presynaptic caspase-3 activation in enhancing presynaptic complement tagging and subsequent microglial phagocytosis, we employed an optogenetic approach. This approach allowed us to selectively activate the caspase cascade in specific neuronal compartments. Considering that the cytochrome c release to caspase-9 activation cascade is the possible upstream of presynaptic caspase-3 activation (Supplementary Fig. 3d), we used the opto-casp9_AtCRY2-PHR-casp9 (CRY2-casp9) system. In this system, caspase-9 activation is initiated by domain oligomerization upon exposure to blue light (Fig. 3a), which subsequently activates downstream caspase-3²³. CRY2-casp9 was introduced to neurons via the hSyn promoter and activated at an individual presynaptic level using a patterned illumination system (Fig. 3b, arrowheads). Intriguingly, activation of caspase-9 and caspase-3 was observed not only at the stimulated presynapse but also in proximal presynapses along the same axon (Fig. 3b; Supplementary Fig. 10a).

Caspase-9 activation could lead to the cleavage of both caspase-7 and caspase-3, which prompted us to investigate the involvement of caspase-7. However, we did not detect cleaved caspase-7 signals in photoactivated neurons (Supplementary Fig. 10a). Consistent with previous reports^{5,6,24}, our findings suggest that caspase-3 plays a major role in neuronal local apoptosis.

We proceeded to examine whether CRY2-casp9-induced caspase-3 activation induces synaptic tagging by complement. After applying C1qA and stimulating presynapses with blue light, we fixed and immunostained the cultured neurons to identify presynapses and the presence of C1qA (Fig. 3c). The C1qA signal in presynapses significantly

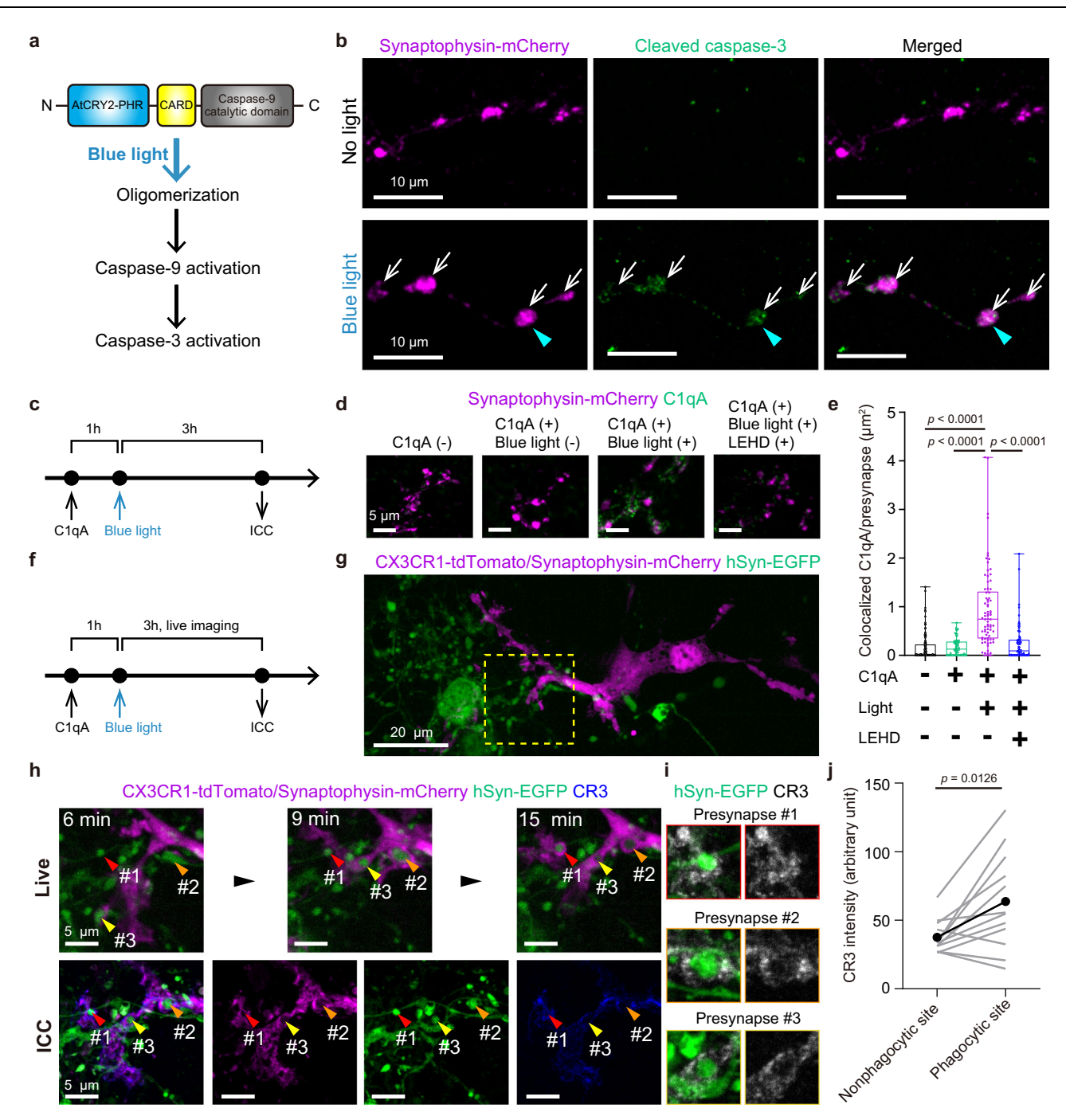


Fig. 3 | **Optogenetic caspase-3 activation induces complement-dependent synaptic phagocytosis. a** Diagram illustrating optic induction of caspase activation. **b** Images showing cleaved caspase-3 signals at presynapses (arrows) following blue light stimulation of a single presynaptic bouton (arrowhead). The experiment was independently repeated 4 times with similar results. **c** Timeline showing caspase activation and synaptic complement tagging identification by immunocytochemistry (ICC). **d** Images showing C1qA and presynapses. The stimulated points are outside the ROL **e** Proportion of C1qA area in a presynaptic bouton. LEHD refers to the caspase-9 inhibitor Z-LEHD-FMK TFA. n = 119, 63, 78, 74 presynapses from 3 independent experiments, Dunn's test after one-way ANOVA on ranks. Box plots are defined as follows: the central line within the box represents the median (50th percentile), while the bounds of the box represent the 25th and 75th percentiles.

The whiskers extend to the minimum and maximum values. All individual data points are plotted. **f** Timeline showing caspase activation, live imaging of microglial synaptic phagocytosis, and ICC detection of complement receptors. **g** A representative image of microglia–neuron interactions. **h** Magnified images from **g** (dashed-line square). Top: live images of microglial synaptic phagocytosis. The elapsed time from the start of live imaging is shown in the upper left corner of each image. Bottom: ICC evidence of CR3 surrounding phagocytosed synapses. **i** Magnified images from **h** detailing phagocytosed presynapses and CR3. **j** Comparison of CR3 intensity around phagocytosed synapses (phagocytic site) and at other sites in microglial processes (nonphagocytic site). Plots from the same region are connected with a line. n = 12 presynapses from 7 independent experiments, two-sided paired t test. Source data are provided as a Source Data file.

increased exclusively upon CRY2-casp9 activation in the presence of C1qA, which was reversed to control levels by the caspase-9 inhibitor Z-LEHD-FMK TFA (Fig. 3d, e). This finding highlights that presynaptic caspase-3 activation alone is sufficient for complement tagging.

Subsequently, we examined the capacity of CRY2-casp9-driven caspase-3 activation to amplify complement-dependent synaptic phagocytosis. We began with live imaging of neurons and microglia (Fig. 3f, g) after C1qA application and blue light stimulation of targeted synapses

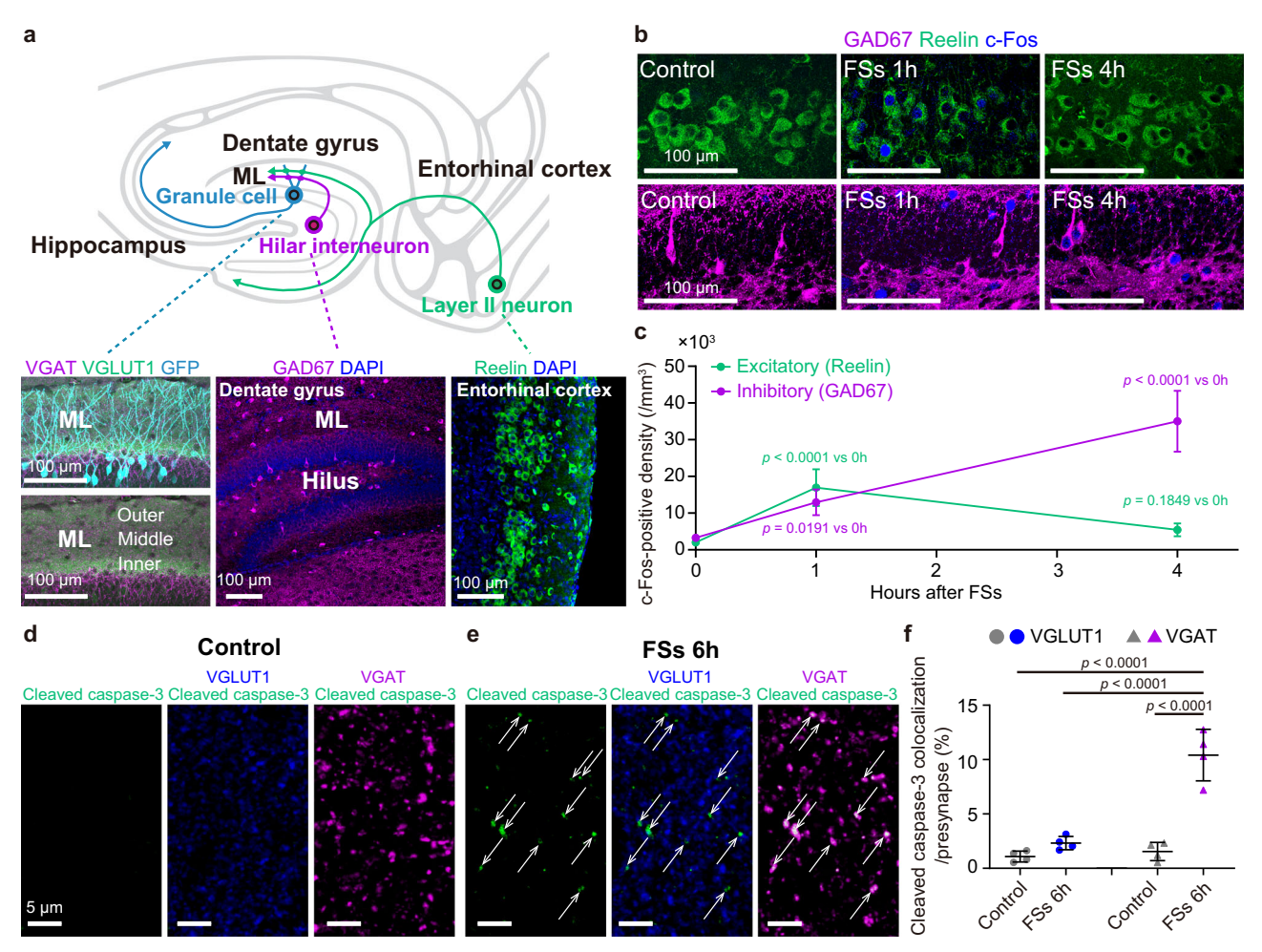


Fig. 4 | **Caspase-3** is specifically activated at inhibitory synapses after febrile seizures (FSs). a Dentate granule cells receive both excitatory and inhibitory neuronal inputs in the middle molecular layer (ML) of the dentate gyrus. The experiment was independently repeated 35 times with similar results. **b** Immunohistochemical images showing c-Fos together with excitatory (Reelin) or inhibitory (GAD67) neurons 1 hour and 4 hours after FSs. **c** c-Fos-positive neuron density at each time point after FSs. Mean \pm SD, n = 5 (inhibitory, 0 h), 6 (inhibitory,

1 h), 6 (inhibitory, 4 h), 6 (excitatory, 0 h), 6 (excitatory, 1 h), 6 (excitatory, 4 h) mice, Dunnett's test after one-way ANOVA. **d**, **e** Immunohistochemical images of cleaved caspase-3 with excitatory (VGLUT1) or inhibitory (VGAT) presynapses 6 hours after FSs. Arrows indicate synapses with colocalized cleaved caspase-3 signals. **f** Proportion of excitatory and inhibitory presynapses with colocalized cleaved caspase-3 6 hours after FSs. Mean \pm SD, n=4 mice, Tukey's test after one-way ANOVA. Source data are provided as a Source Data file.

(Fig. 3h, arrowheads). After observing presynaptic phagocytosis, we fixed the samples to ensure that the observed phagocytosis was indeed complement-dependent (Fig. 3h). We particularly identified the presence of the C3 receptor (CR3), which recognizes activated C3, a downstream molecule of C1q, through immunostaining (Fig. 3h, i). The CR3 fluorescence intensity was markedly increased in regions where microglial processes grabbed presynapses (phagocytic site), implying complement-dependent phagocytosis of caspase-3-activated presynapses (Fig. 3i, j). Notably, microglia selectively phagocytosed presynapses without shearing axons after caspase-3 activation with CRY2-casp9 (Fig. 3h).

Next, we investigated whether photoactivation of CRY2-casp9 induces synaptic phagocytosis on its own. We have performed live imaging of synaptic phagocytosis by microglia following photoactivation of CRY2-casp9 with or without ClqA addition. We confirmed that the addition of ClqA significantly decreases the latency to CRY2-casp9-induced synaptic phagocytosis (Supplementary Fig. 10b, c). In conclusion, photoactivation of CRY2-casp9 alone induces synaptic phagocytosis, which is further accelerated by synaptic accumulation of Clq.

Finally, we examined the characteristics of presynaptic proteins that are phagocytosed in a caspase-3-dependent manner, specifically whether microglia phagocytose presynapses that form synapses. However, it is challenging to determine whether phagocytosed

synaptophysin-mCherry puncta formed synapses by immunostaining after live imaging due to the positional changes of neurites caused by astrocytic movement. Therefore, we examined the colocalization of postsynaptic markers with synaptophysin-mCherry that remained on the neuronal side after partial phagocytosis (trogocytosis) of synaptophysin-mCherry. Our results show that 80% of the remaining synaptophysin-mCherry puncta are colocalized with excitatory or inhibitory postsynapses (Supplementary Fig. 11a, b). This finding is consistent with additional data indicating that about 85% of all synaptophysin-mCherry in the field of view formed synapses (Supplementary Fig. 11c, d). Furthermore, we confirmed that postsynaptic molecules are not incorporated into microglia after live imaging of synaptophysin-mCherry phagocytosis (Supplementary Fig. 11e, f).

These results suggest that the majority of mCherry-labeled synaptophysin puncta are associated with postsynapses and that microglia selectively phagocytose presynaptic components. While we acknowledge that approximately 20% of synaptophysin-mCherry puncta may not correspond to true presynapses and could be mere axonal boutons, the high percentage of colocalization provides a reasonable level of accuracy for referring to these puncta as presynapses.

The results presented in Figs. 1 to 3 confirmed that presynaptic caspase-3 activation in response to increased neuronal activity

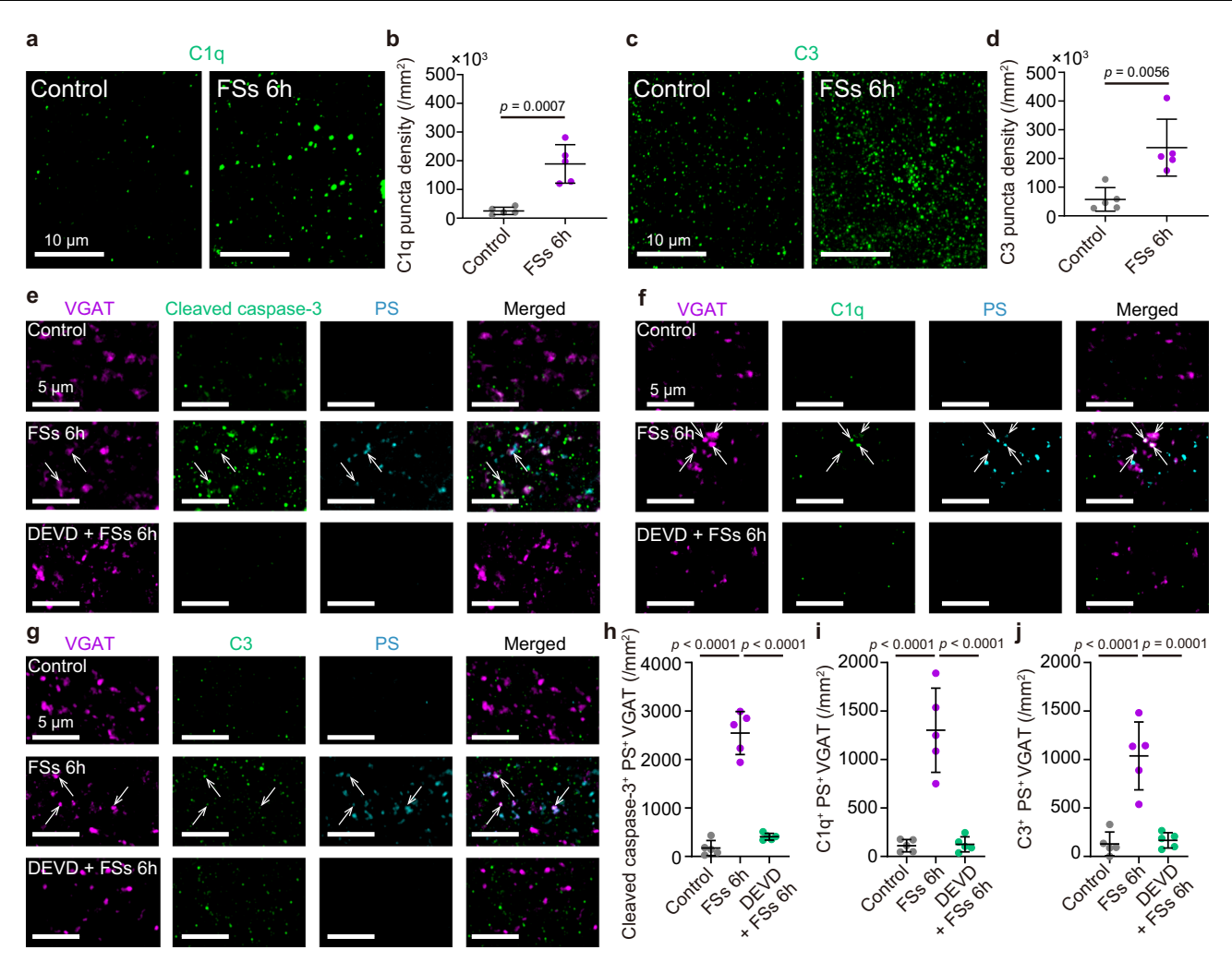


Fig. 5 | **Inhibitory synaptic caspase-3 activation leads to complement tagging. a, c** Immunohistochemical images of C1q and C3 in the middle molecular layer 6 hours after febrile seizures (FSs). **b, d** Density of C1q and C3 puncta in the middle molecular layer 6 hours after FSs. Mean \pm SD, n=5 mice, two-sided unpaired t test. **e-g** Images displaying colocalized inhibitory presynapses with PSVue (PS) and

cleaved caspase-3 or C1q or C3 6 hours after FSs (arrows). DEVD refers to the caspase-3 inhibitor Z-DEVD-FMK. \mathbf{h} - \mathbf{j} Density of inhibitory presynapses colocalized with PSVue and cleaved caspase-3 or C1q or C3 6 hours after FSs. Mean \pm SD, n = 5 mice, Tukey's test after one-way ANOVA. Source data are provided as a Source Data file.

promotes the C1q tagging of presynapses, subsequently facilitating microglial phagocytosis.

Localized caspase-3 activation after febrile seizures (FSs) promotes inhibitory synaptic tagging by complement

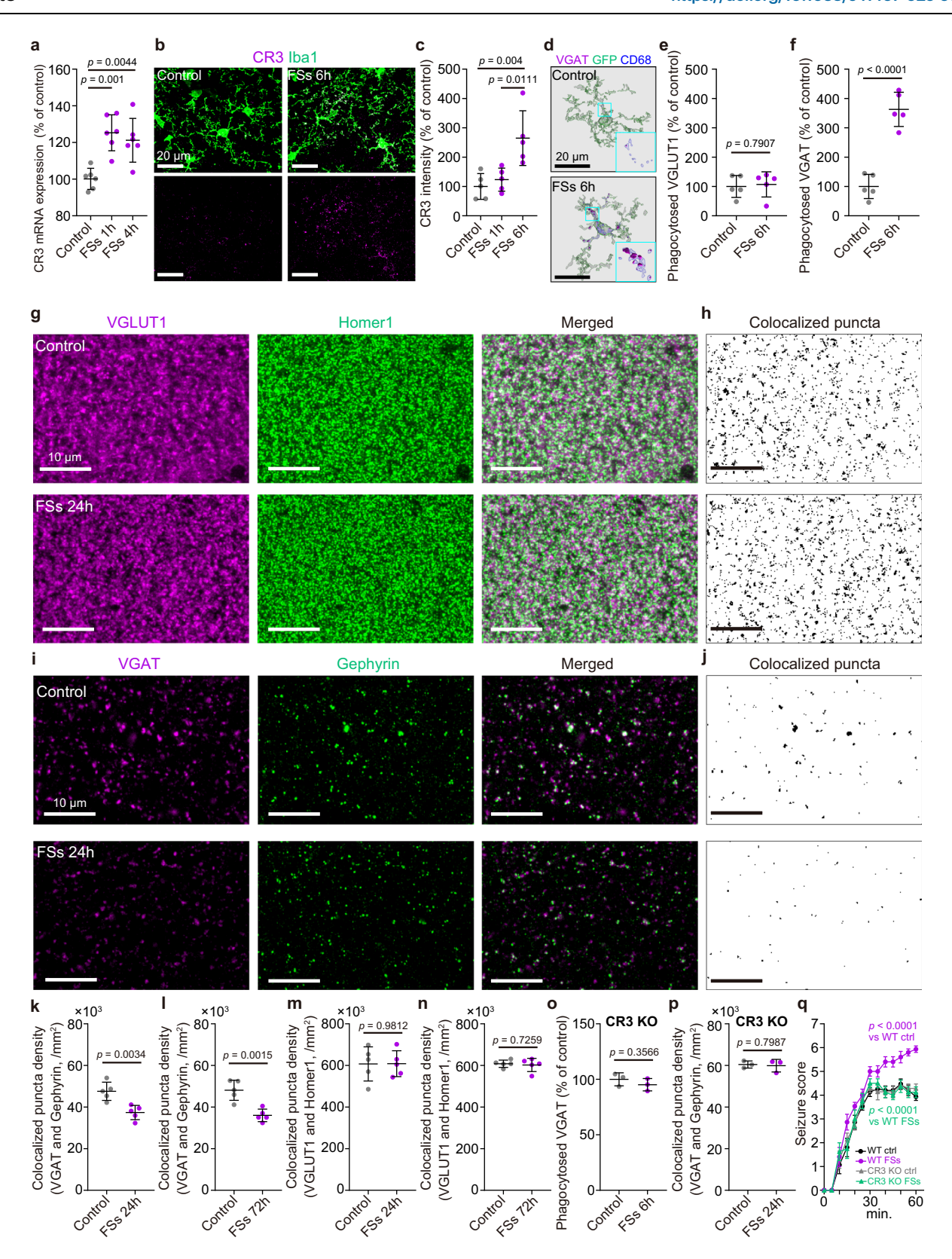
We employed an FS mouse model to understand how synaptic phagocytosis facilitated by nonapoptotic caspase-3 activation affects neuronal circuit remodeling. Previous studies have suggested that FSs result in increased neuronal activity and complement pathway dysregulation^{25,26}. Our focus was presynapses projecting to the dentate granule cells in the hippocampus, recognized as the seizure focus in the FS model (Fig. 4a). In the middle molecular layer of the dentate gyrus, granule cell dendrites receive both excitatory projections from Reelin-positive cells in layer II of the entorhinal cortex and inhibitory projections from interneurons in the hilus (Fig. 4a). First, we assessed neuronal activity after FSs by evaluating the proportion of c-Fospositive cells (Fig. 4b, c). Remarkably, an increase in c-Fos-positive cell density was evident in Reelin-positive cells 1 hour after FSs, which returned to control levels 3 hours later. In contrast, the density of c-Fos-positive interneurons continued to rise for at least 4 hours after FSs (Fig. 4b, c).

Subsequently, we evaluated whether neuronal activation after FSs leads to caspase-3 activation at presynapses. A notable increase in

cleaved caspase-3 immunostained signals, which predominantly colocalized with inhibitory presynapses, was evident 6 hours after FSs (Fig. 4d-f). This finding supports the notion that prolonged neuronal activity can induce presynaptic caspase-3 activation. Concurrently, at this 6-hour mark, both C1q and C3 expression levels increased, as evidenced by immunohistochemistry (Fig. 5a-d). We also observed a significant increase in the colocalization of inhibitory presynapses with Clq or C3 and externalized PS detected by PSVue (Fig. 5e-j). Notably, introducing the caspase-3 inhibitor Z-DEVD-FMK 15 minutes prior to seizure induction reduced this colocalization to baseline levels (Fig. 5e-j). It should be noted that the caspase-3 inhibitor did not affect FSs induction, as latencies to seizures (time to induce clonic seizures after applying hyperthermia) were comparable between FSs and DEVD + FSs groups (FSs: 511.4 ± 49.8 seconds; DEVD + FSs: 502.2 ± 41.7 seconds, mean \pm SD, n = 5 mice, P > 0.05, unpaired t test). Overall, these results suggest that after FSs, caspase-3 activation facilitates inhibitory presynaptic tagging by complement, possibly via PS exposure.

After FSs, microglia phagocytose inhibitory presynapses in a complement-dependent fashion

The prominent tagging of inhibitory synapses by complement after FSs led us to further examine microglial synaptic phagocytosis. A rise in CR3 mRNA (Fig. 6a) and subsequent protein expression (Fig. 6b, c)



within microglia 6 hours after FSs was apparent, suggesting enhanced complement recognition. Additionally, microglia appeared to interact with cleaved caspase-3-positive inhibitory presynapses 6 hours after FSs (Supplementary Fig. 12a, b), implying a possible role of caspase-3 in synapse–microglia interplay. Immunohistochemical analyses revealed an increase in the phagocytosis of inhibitory presynapses after FSs (Fig. 6d, f), while phagocytosis of inhibitory postsynapses and

excitatory synapses remained stable (Fig. 6e; Supplementary Fig. 12c, d). Aligning with these findings, only the density of inhibitory synapses declined 24 and 72 hours after FSs (Fig. 6g–n). We verified that this microglial synaptic phagocytosis was complement-dependent, as both the increase in phagocytosis and the reduction in inhibitory synapse density after FSs were nullified in CR3 knockout mice (Fig. 6o, p). Consistent with these results, inhibitory synaptic

Fig. 6 | After febrile seizures (FSs), microglia phagocytose inhibitory synapses through a complement cascade. a CR3 mRNA levels in hippocampal extracts 1 hour and 4 hours after FSs. β-actin was used as an internal standard. Mean \pm SD, n=6 mice, Tukey's test after one-way ANOVA. **b** Immunohistochemical images of microglia (Iba1) and CR3 in the middle molecular layer 6 hours after FSs. **c** Immunostained CR3 intensity in the middle molecular layer. Mean \pm SD, n=5 mice, Tukey's test after one-way ANOVA. **d** Representative 3D reconstructed images of microglia (CX3CR1-GFP), lysosomes (CD68) and inhibitory presynapses (VGAT) 6 hours after FSs. **e**, **f** Excitatory (VGLUT1) and inhibitory (VGAT) presynaptic volume phagocytosed by microglia 6 hours after FSs. Mean \pm SD, n=5 mice, two-sided unpaired t test. **g**, **i** Immunohistochemical images of excitatory

synapses (pre: VGLUT1; post: Homer1) and inhibitory synapses (pre: VGAT; post: Gephyrin) in the middle molecular layer at 24 hours after FSs. **h**, **j** Images of colocalized synaptic puncta corresponding to (**g**) and (**i**). **k**–**n** Colocalized synaptic puncta density (as shown in images of (**h**) and (**j**)) 24 hours and 72 hours after FSs shown as % of control. Mean \pm SD, n = 5 mice, two-sided unpaired t test. **o** Inhibitory presynaptic (VGAT) volume phagocytosed by microglia in CR3 knockout (KO) mice 6 hours after FSs. Mean \pm SD, n = 3 mice, two-sided unpaired t test. **q** Inhibitory synapse density in CR3 KO mice 24 hours after FSs. Mean \pm SD, n = 3 mice, two-sided unpaired t test. **q** Seizure scores following kainic acid injection 72 hours after FSs. Mean \pm SD, n = 15, 15, 8, 7 mice, two-way repeated-measures ANOVA (Time x Group Factor). Source data are provided as a Source Data file.

phagocytosis by astrocytes was not increased after FSs, suggesting that the reduction in inhibitory synapses after FSs was mainly attributed to microglia (Supplementary Fig. 13).

Finally, we examined how microglial synaptic phagocytosis influences neuronal circuit excitability. Three days after FSs, at a point when inhibitory synapse density remained decreased (Fig. 6l, n), we introduced kainic acid-triggered acute seizures in mice. Seizure scores were significantly higher in mice that had previous FSs, indicating increased circuit excitability (Fig. 6q). However, this increase was suppressed in CR3 knockout mice. Given that there was no discernible inhibitory neuronal cell death after FSs (Supplementary Fig. 14), these findings suggest that the decrease in inhibitory synapses 24 hours after FSs underpins the increased circuit excitability.

Discussion

Here, we describe a culture system for live imaging of synapse–microglia interactions. Experiments using this system revealed two main insights. First, increased neuronal activity triggers nonapoptotic caspase-3 activation locally at presynapses. Second, this caspase-3 activation leads to subsequent presynaptic tagging by complement, which results in microglial synaptic phagocytosis. Additionally, microglial synaptic pruning via this nonapoptotic caspase-3 activation alters neuronal excitability in a mouse model of FSs. Hence, our results identified a role of nonapoptotic caspase-3 activation in synaptic pruning and circuit remodeling (Fig. 7).

Our culture system enabled the real-time observation of microglial synaptic phagocytosis without axonal shearing. Since this synapse-specific phagocytosis is a distinguishing feature of synaptic pruning prompted by local apoptosis, future research should determine whether similar phagocytic processes occur in vivo. Although in vivo live imaging of synaptic phagocytosis was recently reported²⁷, studying the phagocytic mechanisms evident in our culture system may be challenging due to resolution and multicolor imaging constraints. Synapse-specific phagocytosis might be regulated by mechanisms distinct from traditional phagocytosis, where phagocytes engulf whole cells^{28–31}. We propose the involvement of membrane fusion, as synaptic proteins phagocytosed by microglia were detected in clathrin-coated vesicles¹⁰. Live imaging of the cytoskeleton and clathrin during synaptic phagocytosis may elucidate the intricate molecular mechanisms involved in this process. Our study revealed increased complement receptor expression in microglial processes during synaptic phagocytosis. Given the importance of local translation at peripheral processes for efficient microglial synaptic phagocytosis¹², complement receptor translation in these locations might aid synapse-specific phagocytosis.

Interestingly, while a previous study suggested that the axon terminals from less active neurons are preferentially phagocytosed in the developing lateral geniculate nucleus in a complement-dependent manner⁹, we found that microglia preferentially phagocytose synapses from highly active neurons. We further showed that reduced neuronal activity decreased synaptic phagocytosis by microglia while synaptic caspase-3 activation was not affected. These results suggest the

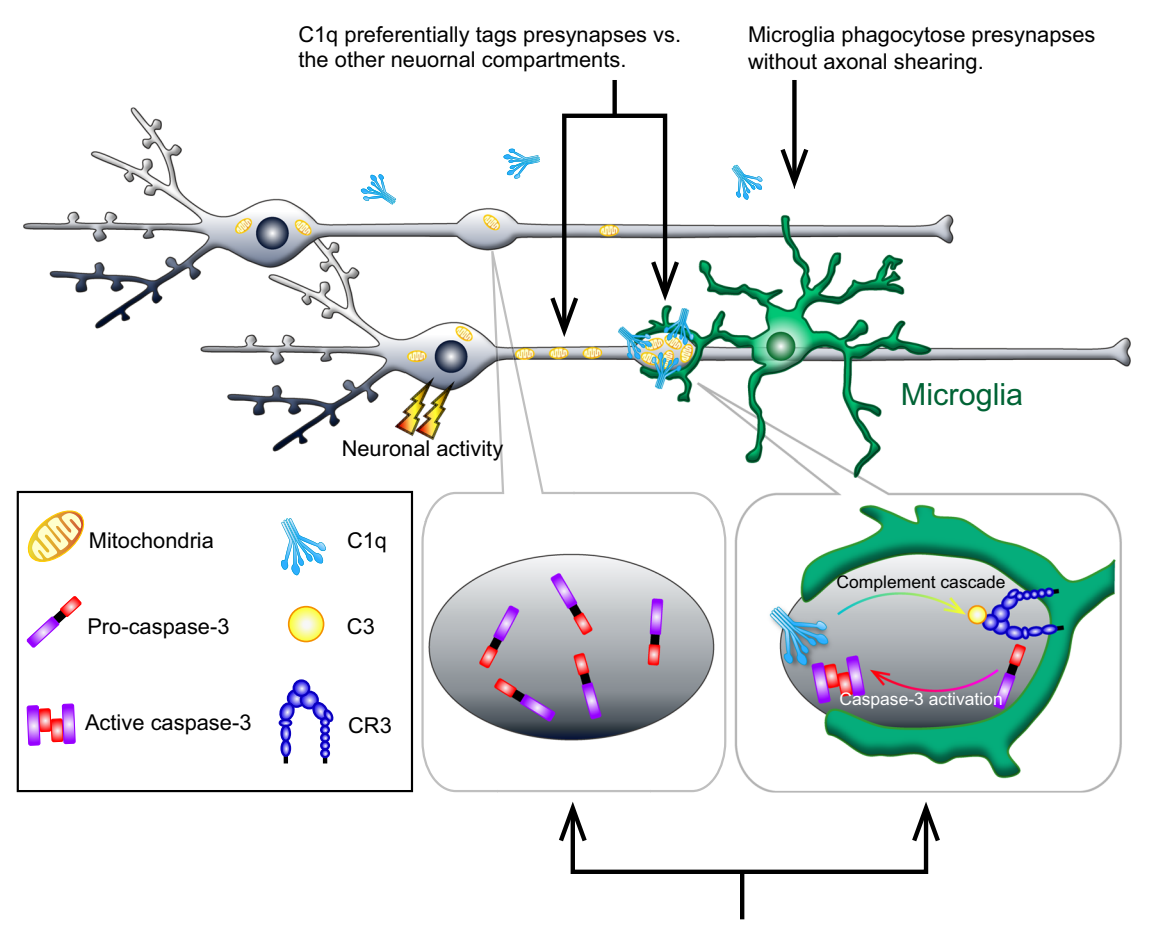
distinct mechanisms of synaptic tagging by complement between neuronal circuit formation and modulation.

We found that increased neuronal activity leads to presynaptic caspase-3 activation, possibly due to calcium influx related to this increased activity. Considering that VGCCs allow calcium ion influx into neurons after membrane depolarization¹³ and that excessive calcium ion influx into mitochondria can lead to cytochrome c release, activating procaspase-314,32, it is possible that increased neuronal activity upregulates apoptotic protein expression via VGCC activation. Notably, since prior research reported upregulated VGCC expression in inhibitory hippocampal neurons after pilocarpine-induced seizures³³, it is possible that a similar mechanism takes place in our FS model. It has also been suggested that pro-brain-derived neurotropic factor, which is released by neurons in an activity-dependent manner, promotes cytochrome c release from mitochondria and caspase-3 activation³⁴. Moreover, the activation of caspase-3 being limited to the presynapse might be connected to the distribution of neuronal mitochondria, given that these energy hubs are transported from the soma to energy-demanding presynapses³⁵.

Our observations highlight that caspase-3 activation extends to neighboring presynapses within the same axons. This propagation of caspase-3 activation along axons may be mediated by motor proteins and the cytoskeleton¹. However, our results indicate that complement tagging and microglial phagocytosis remain confined to specific presynapses. Determining the specifics of this process, which might involve factors such as caspase-3 activity levels and synapse coverage by astrocytic processes or the extracellular matrix, requires further exploration. Nonetheless, the lower number of microglia compared to presynapses and the constraints of live imaging duration in our in vitro experiments might have led to overlooking certain phagocytic events.

We found that localized caspase-3 activation at presynapses did not result in neuronal death. One potential factor that enables this localized and transient activation is the inhibition of caspase-3 by inhibitor of apoptosis proteins (IAPs)^{1,36}. Following increased neuronal activity, the expression and activation of IAPs could occur in the neuronal soma, which is in consistent with case of local caspase activation observed during dendrite elimination⁶. Employing mSCAT3 could verify localized and transient caspase-3 activation in vitro, although further validation is warranted due to variations in FRET recovery speed based on the linked protein.

The DEVD sequence in synaptophysin-mSCAT3 could also be cleaved by caspase-7, because caspase-9 activation could promote the cleavage of both caspase-7 and caspase-3. However, previous reports have shown lower expression levels and activation of caspase-7 than caspase-3 in hippocampal neurons^{5,6,24}. Additionally, it has been demonstrated that local apoptosis at spines and dendrites is mainly attributed to caspase-3^{5,6,24}. In the current research, we confirmed that caspase-7 would not be cleaved following local caspase-9 activation (Supplementary Fig. 10a). These findings suggest that synaptophysin-mSCAT3 primarily reflects the activation of caspase-3 following increased neuronal activity. While we acknowledge the possibility that caspase-7 might also contribute to the cleavage of synaptophysin-mSCAT3 under certain conditions, our current data strongly indicate



Neuronal activity induces caspase-3 activation and C1g localization at presynapses.

Fig. 7 | **Graphical abstract of the present research.** Increased neuronal activity induces nonapoptotic caspase activation at presynapses, probably via mitochondrial accumulation. Caspase activation causes synaptic tagging by Clq, leading to

C3 localization at presynapses. Microglial CR3 recognizes C3, inducing synapse-specific phagocytosis by microglia.

that caspase-3 is the primary driver in our experimental system. Future studies may further elucidate the specific contributions of each caspase in synaptic environments.

The exact mechanism by which caspase-3 activation promotes synaptic tagging by complement remains elusive. Some studies reported the enhancement of PS externalization by caspase-3 activation²¹ and the subsequent binding of PS to Clq²². We found that increased neuronal activity enhanced synaptic PS externalization both in vitro and in vivo. However, other pathways beyond caspase-3 activation can also promote PS externalization, and some research challenges the notion of Clq binding to PS³⁷.

An in-depth examination of upregulated molecules in the activated caspase-3-positive synaptosome may help identify the intermediary linking synapses and C1q. The current study suggests that stronger and longer binding of C1q is crucial for the activation of the complement pathway triggered by C1q, which is facilitated by increased neuronal activity, subsequent caspase activation, and PS presentation. This might explain the presence of C1q puncta without inducing microglial phagocytosis in the brain (Fig. 5i).

We hypothesize that CIq not colocalized with VGAT may be transiently attaching and detaching from other neuronal compartments or being incorporated into glial cells. Therefore, only those CIq puncta that are strongly and irreversibly tagged, particularly when PS is present, are likely to be detected by microglia and targeted for phagocytosis.

In our FS mouse model, both excitatory and inhibitory neurons displayed distinct activity patterns following FSs. The sustained increase in inhibitory neuronal activity could act to recurrently suppress the activity of excitatory neurons, as seen in pilocarpine-induced seizure models^{38,39}. Given the specificity of caspase-3 activation, C1q tagging, and microglial phagocytosis of inhibitory presynapses after FSs, constant neuronal activity might be a precursor to caspase-3 activation. However, there are claims suggesting that the VGCC and mitochondrial distributions differ between excitatory and inhibitory neurons^{40,41}. Thus, further studies are necessary to explore the cell type specificity of caspase-3 activation in response to increased neuronal activity.

While our study provides insights into synaptic phagocytosis driven by localized caspase-3 activation, the neuronal activity observed both in vitro and in the FS model might be more intense than regular neuronal activity. Therefore, evaluating the relevance of our discoveries in other contexts, such as during brain development and synaptic plasticity, is crucial. Nonetheless, the data from our in vivo seizure model emphasize the importance of the mechanisms we have detailed in situations with increased neuronal activity. Recognizing these limitations is essential for a comprehensive understanding of the role of localized nonapoptotic caspase activity in circuit remodeling both in physiological and pathological conditions.

Methods

Animals

All animal experiments were conducted with the approval of the Animal Experiment Ethics Committee of the University of Tokyo (approval

numbers, P4-2, P4-4) and in accordance with the University of Tokyo's guidelines for the welfare of experimental animals, C57BL/61 mice (SLC), Thv1-GFP mice (Tg(Thv1-EGFP)MIrs/I, Stock No: 007788, The Jackson Laboratory), CX3CR1-GFP (B6.129P2(Cg)-Cx3cr1^{tm1Litt}/I, Stock No: 005582, The Jackson Laboratory), CR3 KO mice (B6.129S4-Itgam^{tm1Myd}/J, Stock No: 003991, The Jackson Laboratory), CX3CR1^{CreER} mice (B6.129P2(Cg)-Cx3cr1tm2.1(cre/ERT2)Jung/J, Stock No: 020940, The Jackson Laboratory) and Ai14 mice (B6;129S6-Gt(ROSA)26Sortm14(CAG-tdTomato)Hze/ J, Stock No: 007908, The Jackson Laboratory) were purchased. To specifically express tdTomato in microglia, Ai14 mice were crossed with CX3CR1^{CreER} mice to generate CX3CR1^{+/CreER}::Ai14^{+/-} mice. Mlc1-tTA::tetO-YC-Nano50 mice were kindly gifted by Dr. Kanemaru (Nihon University School of Medicine, Tokyo). All mice were maintained on a 12-hour light/dark cycle at 24 °C with 50-60% humidity and provided with unlimited food and water. At the end of experiments, mice were anesthetized with isoflurane in a bell jar, followed by transcardial perfusion and tissue collection.

Neuron-glia coculture

For preparation of glial cocultures, P1–4 mice were anesthetized with ice, and brains were removed and placed into ice-cold Hank's balanced salt solution (HBSS). The brains were rapidly dissected using fine scissors and forceps and the cortex was separated from the meninges and isolated under a dissection microscope. Cortices were collected in ice-cold HBSS and kept on ice until the brains had been removed from all mice. Tissues were minced using scalpels and incubated with 0.25% trypsin (Nacalai, #35555-54) and 0.01% DNase I (Roche, #10104159001) in HBSS at 37 °C for 40 minutes. Heat-inactivated fetal bovine serum (FBS; Gibco, #10437028) was added to stop trypsinization, and tissues were centrifuged for 10 minutes at $136 \times g$ at room temperature. The tissues were then dissociated into a single-cell suspension in culture medium containing 10% FBS and 1% penicillin-streptomycin (Nacalai, #09367-34) in Dulbecco's modified Eagle medium (DMEM; Gibco, #10569010). Single cells were filtered through a 100-um-pore cell strainer and plated in a poly-D-lysine (PDL: 10 ug/mL, Sigma, #P6407)coated T75 flask (Falcon, #353136). The flask was placed in a 35 °C, 5% CO₂ incubator. The medium was changed the day after plating of the mixed cortical cells and every 3 days thereafter. After culturing for 2 weeks, cortical microglia and astrocytes were transferred to 35 mm glass-bottom dishes (IWAKI, #11-0606) as follows. The cultures were rinsed twice with 10 mL of 0.1 M phosphate-buffered saline (PBS) and incubated with 0.05% trypsin-ethylenediaminetetraacetic acid (EDTA; Gibco, #25200072) at 35 °C for 10 minutes. Detached cells were collected and centrifuged for 5 minutes at 95 × g at room temperature. After the supernatant was discarded, the cells were processed into a single-cell suspension in culture medium, filtered through a 100-μm-pore cell strainer and plated onto PDL (10 μg/mL)-coated 35 mm glass-bottom dishes at a density of 1.5×10^5 cells/dish. Secondary cultures were placed in a 35 °C, 5% CO2 incubator, and the medium was changed the day after transfer of the mixed cortical cells and every 3 days thereafter.

After 7 days, hippocampal neurons were added to secondary glial cultures. P1 mice were anesthetized with ice, and brains were removed and placed in warmed HBSS. Using fine scissors and forceps, brains were rapidly dissected, and the hippocampi were separated from the meninges and isolated under a dissection microscope. Hippocampi were collected in warmed HBSS and kept until the brains were removed from all mice. Tissues were minced with scalpels and incubated with 0.05% trypsin-EDTA in HBSS at 37 °C for 15 minutes, followed by incubation with 0.01% DNase I in HBSS at room temperature for 5 minutes. Tissues were washed with HBSS 3 times for 5 minutes each time and fragmented with Pasteur pipettes in neurobasal medium (Gibco, #12348017) containing 2% B27 supplement (Gibco, #17504-044), 0.5 mM glutamine solution (Nacalai, #16948-04), 25 μ M glutamate (MW 147.13 g/mol), 0.5% penicillin—

streptomycin, 1 mM HEPES (MW 238.3 g/mol, Sigma, H3375), and 10% heat-inactivated horse serum (Gibco, #26050088). Single cells were filtered through a 40-µm-pore cell strainer and centrifuged for 10 minutes at 54 × g at room temperature. After the supernatant was discarded, the cells were processed into a single-cell suspension in DMEM containing 10% FBS and plated on secondary glial cultures at a density of 2 × 10⁵ cells/dish. Cultures were placed in a 35 °C, 5% CO₂ incubator, and the medium was changed the day after plating hippocampal neurons and every 3 days thereafter. For neuron gene transduction, each adeno-associated virus (AAV) was added to the culture medium at a multiplicity of infection (MOI) of 3 × 10⁴ 1 weeks after plating hippocampal neurons.

For glial cocultures derived from CX3CR1 $^{+/CreER}$::Ai14 $^{+/-}$ mice, 4-hydroxy tamoxifen (final concentration: $2\,\mu M$) was added to the culture medium at 9–14 days in vitro (DIV) to induce Cre-dependent tdTomato expression in microglia.

Quantitative real-time PCR (RT-qPCR) in vitro

RNA was extracted from MACS-sorted microglia using an RNeasy Plus Mini Kit (Oiagen) according to the manufacturer's instructions. The RNA samples were reverse-transcribed into cDNA using a SuperScript VILO cDNA Synthesis Kit (Invitrogen), and the 1/10 of the cDNA was amplified with the THUNDERBIRD® Next SYBR™ qPCR Mix (TOYOBO) using a QuantStudio™ 3 Real-Time PCR (Applied Biosystems). Triplicate Ct values were averaged, and data are shown as respective to the GAPDH using the Ct delta method ($2^{-\Delta\Delta Ct}$). Primer sets were as follows: GAPDH, 5'catcactgccaccagaagactg-3' and 5'-atgccagtgagcttcccgttcag-3', P2Y12, 5'cattgaccgctacctgaagacc-3' and 5'-gcctcctgttggtgagaatcatg-3', CD11b, 5'-a tggacgctgatggcaatacc-3' and 5'-tccccattcacgtctccca-3', Tmem119, 5'-cc tactctgtgtcactcccg-3' and 5'-cacgtactgccggaagaaatc-3', Hexb, 5'-cgc agtccccgcgtag-3' and 5'-agttgtaatatcgccgaaacgc-3', Cx3cr1, 5'-gagtatgacg attctgctgagg-3' and 5'-cagaccgaacgtgaagacgag-3', Ccr2, 5'-aggagccatacctgtaaatgcc-3' and 5'-tgtggtgaatccaatgccct-3', Ly6C, 5'-gtgtgc agaaagagctcagg-3' and 5'-gaaaggcactgacgggtctt-3'.

Virus production

Plasmid design. For pAAV-hSyn-hM3Dq-T2A-H2B-GFP and pAAVhSvn-hM4Di-T2A-H2B-GFP, the coding sequences of T2A and H2B-GFP were PCR-amplified from pAAV-tetO-GFP-2A-bPAC⁴² and pEGFP-N1-H2B-GFP (Addgene, #11680), respectively. Then, both fragments were ligated into the pAAV-hSyn-hM3D(Gq)-mCherry vector and pAAV-hSyn-hM4D(Gi)-mCherry vector (Addgene, #50474 and #50475) using In-Fusion (Takara, #639648). For pAAV-hSyn-Mito-DsRed, the coding sequences of Mito-DsRed were PCR-amplified from the pDsRed2-Mito vector (TakaRa, #632421), and the fragments were ligated into the pAAV-hSyn-EGFP vector (Addgene, #50465) using In-Fusion. For pAAV-hSyn-synaptophysin-mCherry, the coding sequences of synaptophysin and mCherry were PCR-amplified from a mouse cDNA library and pAAV-CaMKIIa-hM3D(Gq)-mCherry (Addgene, #50476), respectively. Both fragments were ligated into the pAAV-hSyn-EGFP vector using In-Fusion. For pAAV-hSyn-membrane-iRFP, the coding sequences of membrane-iRFP were PCRamplified from pCMV-Mem-iRFP (Addgene, #59134), and the fragments were ligated into the pAAV-hSyn-EGFP vector using In-Fusion. For pAAV-hSyn-opto-casp9_AtCRY2-PHR-casp9, the coding sequences were PCR-amplified from pcDNA3.1-opto-casp9_AtCRY2-PHRcasp9 (Addgene, #131221), and the fragments were ligated into the pAAV-hSyn-EGFP vector using In-Fusion cloning.

Virus packaging. Recombinant AAVs were generated by triple transfection of the 293 AAV cell line (Cell Biolabs, #AAV-100) with AAVdj rep-cap, pHelper from the AAV-DJ Helper Free Packaging System (Cell Biolabs, #VPK-400-DJ) and pAAV-hSyn-hM3Dq-T2A-H2B-GFP or pAAV-hSyn-hM4Di-T2A-H2B-GFP or pAAV-hSyn-Mito-DsRed or pAAV-hSyn-Synaptophysin-mCherry or pAAV-hSyn-Synaptophysin-mSCAT3 or

pAAV-hSyn-membrane-iRFP or pAAV-hSyn-opto-casp9_AtCRY2-PHR-casp9 or pAAV-hSyn-EGFP using PEI-Max (Polysciences, #24765). AAV vectors were purified using the AAVpro Purification Kit All Serotypes (TaKaRa, #6666). Virus titers were determined by quantitative real-time PCR (RT–qPCR) using the AAV2 ITR primer pair⁴³, Luna Universal qPCR Master Mix (New England Biolabs, #M3003S) or THUNDERBIRD Next SYBR qPCR Mix (TOYOBO, #QPX-201), and the LightCycler qPCR 2.0 system (Roche, #DX400).

Preparation for reagents

Each reagent was purchased and reconstituted as follows: Clozapine *N*-oxide (final: 20 μ M, stock: 20 mM in DMSO) (Tocris, # 4936), Z-DEVD-FMK (final: 10 μ M, stock: 10 mM in DMSO, Adooq, # A13503), BAX channel blocker (final: 2 μ M, stock: 20 mM in DMSO, Santa Cruz, #sc-203524), NS3694 (final: 2 μ M, stock: 20 mM in DMSO, Santa Cruz, #sc-203823) and Z-LEHD-FMK TFA (final: 20 μ M, stock: 20 mM in water) (Selleck, #S7313).

Immunohistochemistry and immunocytochemistry

Antibodies for immunostaining. The following primary antibodies were used: rabbit anti-Iba1 (1:500; Wako, #019-19741), rat anti-CD68 (1:500; Bio-Rad, #MCA1957GA), guinea pig anti-VGLUT1 (1:1000; Synaptic Systems, #135 304), mouse anti-VGLUT1 (1:1000; Synaptic Systems, #135 311), guinea pig anti-VGAT (1:1000; Synaptic Systems, #131 004), mouse anti-VGAT (1:1000; Synaptic Systems, #131 011), rabbit anti-Homer1 (1:500; Synaptic Systems, #160 002), guinea pig anti-Homer1 (1:500; Synaptic Systems, #160 004), rabbit anti-Gephyrin (1:500; Synaptic Systems, #147 008), mouse anti-Reelin (1:500; MBL, #D223-3), mouse anti-GAD67 (1:500; EMD Millipore, #MAB5406B), rabbit anti-c-Fos (1:5000; Synaptic Systems, #226 008), chicken anti-GFP (1:1000; Abcam, #ab13970), rabbit anti-cleaved caspase-3 (1:400; Cell Signaling Technology, #9661), rabbit anti-cleaved caspase-7 (1:1000; Cell Signaling Technology, #8438), rabbit anti-cleaved caspase-9 (1:50; Cell Signaling Technology, #9509), rabbit anti-Clq (1:100; Abcam, #ab182451), rabbit anti-ClqA (1:200; Abcam, #ab155052), rabbit anti-human C3d (1:100; Agilent, #A0063), rat anti-mouse CD11b (1:500; Bio-Rad, #MCA711G), mouse anti-MAP2 (1:1000; EMD Millipore, #MAB378), mouse anti-βIII tubulin (1:200; Abcam, #ab78078), rabbit anti-DsRed (1:1000; Clontech, #632496), mouse anti-RFP (1:1000; MBL, #M155-3), rabbit anti-GFAP (1:1000; Sigma Aldrich, #G9269) and rabbit anti-LAMP1 (1:500; Abcam, #24170). Secondary antibodies conjugated with Alexa Fluor dyes (1:500; Invitrogen, Gaithersburg, MD, USA) were used.

Sample preparation and immunostaining for in vivo experiments.

Experimental mice were anesthetized with isoflurane (Pfizer Inc.) and transcardially perfused with cold PBS, followed by fixation with 4% paraformaldehyde (PFA). Brain samples were incubated with 4% PFA overnight at 4 °C. Coronal sections (100 μm thick) were prepared using a Zero-1 vibratome (Dosaka). The fixed sections were rinsed 3 times with PBS and incubated in PBS, 0.3% Triton X-100, and 5% goat serum at room temperature for 1 hour. The samples were subsequently incubated with primary antibodies in PBS, 0.3% Triton X-100, and 5% goat serum overnight at room temperature. After antibody incubation, the sections were rinsed 3 times with PBS and then incubated with secondary antibodies in PBS, 0.3% Triton X-100, and 5% goat serum overnight at room temperature. Finally, the samples were rinsed 3 times with PBS and mounted on slide glasses with antifade reagent containing DAPI (Nacalai, #12745-74). Complement immunostaining was performed as previously described 9,17 .

Sample preparation and immunostaining for in vitro experiments. Cultured cells were fixed with 4% PFA for 15 minutes at 37 °C and rinsed 3 times with PBS. The samples were incubated in PBS, 0.3% Triton X-100, and 5% goat serum at room temperature for 1 hour and then

subsequently incubated with primary antibodies in PBS, 0.3% Triton X-100, and 5% goat serum overnight at 4 °C. The samples were rinsed with PBS 3 times and incubated with secondary antibodies in PBS, 0.3% Triton X-100, and 5% goat serum for 4 hours at room temperature. Finally, the samples were rinsed 3 times with PBS and mounted with antifade reagent containing DAPI. Complement immunostaining was performed as previously described 9.17.

TUNEL staining. Cultured cells were fixed with 4% PFA and TUNEL staining was performed according to the manufacturer's instructions of CFTM64OR TUNEL Assay Apoptosis Detection Kit (BTI, #30074). Cells were counterstained with anti-chicken antibody against GFP and DAPI.

Annexin V staining. Cultured cells were washed twice in PBS and incubated in the medium containing Annexin V conjugate (1:100, Invitrogen, #A23204) at 35°C, 5% CO $_2$ for 20 minutes. Then cultured cells were fixed with 4% PFA.

Image acquisition and analysis in vitro

During live imaging, cultured cells were kept at 37 $^{\circ}$ C with 5% CO₂ using a stage top incubator (TOKAI HIT). For surface rendering, the brightness of fluorescence images was adjusted to eliminate noise and halation. The thresholds for binarization and surface rendering were then manually determined based on the signal intensity.

Cleaved caspase-3 localization. Images were captured using a SpinSR10 (Evident) with a 60× objective (NA=1.5) at a resolution of 2048 × 2048 pixels. Z series images were collected with 0.25- μm steps, and 25 Z sections were exported to Imaris Bitplane software. Surface renderings were created for cleaved caspase-3, H2B-GFP (neuronal nuclei), β III-tubulin (axons) and synaptophysin-mCherry (presynapses), and other surface renderings for cleaved caspase-3 colocalized with each neuronal compartment were created. In Fig. 1b, the volumes of colocalized cleaved caspase-3 in a single presynapse were calculated. In Fig. 1d, the volume ratios of cleaved caspase-3 to each neuronal compartment in the field of view were calculated. Neuronal somas were defined as spheres with a radius of 10 μ m from the center of the neuronal nuclei.

Live imaging of caspase-3 activation. Images were captured using a SpinSR10 at a resolution of 2048 \times 2048 pixels. mECFP of synaptophysin-mSCAT3 was excited at 445 nm, and mECFP and mVenus fluorescence intensities were divided by a 445-, 515-, 640-triple dichroic mirror and were simultaneously recorded through 432–483 nm and 527–542 nm band-path filters, respectively. Fifteen Z sections were collected with 0.5- μ m steps using a 60× objective (NA = 1.5). Z sections were stacked, and then the mECFP to mVenus fluorescence emission ratio was calculated using ImageJ software (NIH image).

C1qA-647 localization after hM3Dq activation. Images were captured using a SpinSR10 with a 60× objective (NA = 1.5) at a resolution of 2048 × 2048 pixels. Z series images were collected with 0.25- μm steps, and 25 Z sections were exported to Imaris Bitplane software. Surface renderings were created for C1qA-647, H2B-GFP (neuronal nuclei), β III-tubulin (axons) and synaptophysin-mCherry (presynapses), and other surface renderings for C1qA-647 colocalized with each neuronal compartment were created. The volume ratios of colocalized C1qA-647 to each neuronal compartment in the field of view were calculated. Neuronal somas were defined as spheres with a radius of 10 μm from the center of the neuronal nuclei.

C1qA localization after CRY2-casp9 stimulation. Images were captured using a SpinSR10 with a 60× objective (NA = 1.5) at a resolution of

 2048×2048 pixels. Z series images were collected with 0.25- μ m steps, and 9 Z sections were stacked and analyzed using ImageJ software. Binary images were created for each channel, and the colocalized areas between C1qA and presynapses were measured. The ratios of colocalization to presynapses were calculated.

CR3 intensity after CRY2-casp9 stimulation. Images were captured using a SpinSR10 with a 60× objective (NA = 1.5) at a resolution of 2048 × 2048 pixels. Then, 25 Z series images were collected with 0.25-µm steps and analyzed using ImageJ software. Phagocytosed presynapses were identified by hSyn-EGFP puncta. The phagocytic site was defined as microglial membranes surrounding phagocytosed presynapses detected by CX3CR1-tdTomato signals. All microglial membranes of the same cell other than those at the phagocytic site were defined as the nonphagocytic site. The fluorescence intensities of CR3 at the nonphagocytic site and the phagocytic site were compared. To determine the CR3 intensity, the following calculation was used: (mean CR3 intensity - background intensity)/background intensity.

Synaptic phagocytosis. In Fig. 2d and Supplementary Fig. 9e, images were captured using a SpinSR10 with a $60\times$ objective (NA = 1.5) at a resolution of 2048×2048 pixels. Z series images were collected with 0.33- μ m steps, and 25 Z sections were analyzed using ImageJ software. Binary images were created for each channel, and the colocalized areas between presynapses and microglia were calculated for a single plane. To determine synaptic phagocytosis by microglia, the following calculation was used: volume of internalized presynapses (μ m³)/volume of microglia (μ m³).

In Fig. 2g, i, images were captured using a SpinSR10 with a 60× objective (NA = 1.5) at a resolution of 2048 × 2048 pixels. Thirteen Z sections were collected with 0.33- μ m steps every minute. Images were exported to Imaris Bitplane software, and surface renderings were created for CX3CR1-GFP (microglia), synaptophysin-mCherry (presynapses) and membrane-iRFP (axons). Synaptic phagocytosis was manually detected.

In Fig. 2j, images were captured using an FV1200 (Evident) with a $40\times$ objective (NA = 0.6) at a resolution of 1024×1024 pixels. Ten Z sections were collected with 1μ m steps every 3 minutes. Synaptic phagocytosis was manually identified.

In Supplementary Fig. 1h, j, images were captured using a SpinSR10 with a $60\times$ objective (NA = 1.5) at a resolution of 2048×2048 pixels. 29 Z series images were collected with $0.25\text{-}\mu\text{m}$ steps, and synaptic phagocytosis was analyzed using ImageJ software in the same way as in Fig. 2d.

In Fig. 3f, to avoid the activation of CRY2-casp9 by the 488 nm laser before live imaging, both microglia and presynapses were labeled with red fluorescence. The 561 nm laser was used to determine the field of view. Images were captured using a SpinSR10 with a 60× objective (NA = 1.5) at a resolution of 2048 × 2048 pixels. Fifteen Z series images were collected with 0.5- μ m steps every 3 minutes. Synaptic phagocytosis was manually identified.

Live imaging of mitochondria. Images were captured using a SpinSR10 with a 40× objective (NA = 0.95) at a resolution of 2048 × 2048 pixels. Thirty-one Z series images were collected with 0.3- μ m steps and were analyzed using ImageJ software. Binary images were created for each channel, and the colocalized areas between Mito-DsRed and presynapses were measured at each time point.

c-Fos intensity. Cultured neurons were transduced with AAV-DJ-hM3Dq-T2A-H2B-GFP or AAV-DJ-hM4Di-T2A-H2B-GFP and treated with either DMSO or CNO (20 μ M) in the culture medium. After 2 hours, the samples were fixed with PFA and subjected to immunostaining for c-Fos. Imaging was performed using a SpinSR10 with a 40× objective

(NA = 0.95) at a resolution of 2048 \times 2048, capturing 31 slices with a 0.35- μ m interval. The images were stacked and analyzed using ImageJ software. The nuclei of hM3Dq- or hM4Di-expressing cells were detected by H2B-GFP. To determine the c-Fos intensity, the following calculation was used: (mean c-Fos intensity - background intensity)/ background intensity.

Image acquisition and analysis in vivo

The immunostained samples were analyzed using a Nikon A1-HD25 confocal system.

Cell density. Images were captured with a 20× objective (NA = 0.75) at a resolution of 1024×1024 pixels. Z-series images were collected in 2- μ m steps, and 6 Z-sections (resulting in a total thickness of $10~\mu$ m) were stacked using ImageJ (NIH) for quantification of cell density. These stacked images were used to identify neuronal somas. For each mouse, four separate regions were imaged and processed in this manner, and the average value from these regions was considered as N=1. Multiple mice were used for each experiment, with detailed information provided in the figure legends.

Colocalization assay (cleaved caspase-3, C1q, C3). Images were captured with a $100\times$ objective (NA = 1.49) at a resolution of 1024×1024 pixels. Z-series images were collected in 0.33- μ m steps, and 4 Z-sections (resulting in a total thickness of $1\,\mu$ m) were stacked using ImageJ (NIH) for quantification of colocalization between synapses and cleaved caspase-3, C1q, C3, and phosphatidylserine. For each mouse, six separate regions were imaged and processed in this manner, and the average value from these regions was considered as N=1. Multiple mice were used for each experiment, with detailed information provided in the figure legends. Binary images were created for each channel, and the colocalization between presynapses and cleaved caspase-3, C1q or C3 was measured. The number of colocalized puncta was quantified in the field of view.

CR3 intensity. Images were captured with a 60× objective (NA = 1.35) at a resolution of 1024 × 1024 pixels. Z-series images were collected in 0.5- μ m steps, and 5 Z-sections (resulting in a total thickness of 2 μ m) were stacked using ImageJ (NIH) for quantification of CR3 intensity. The mean intensities of CR3 in Iba1-positive microglia were measured in the stacked images. For each mouse, four separate regions were imaged and processed in this manner, and the average value from these regions was considered as N=1. Multiple mice were used for each experiment, with detailed information provided in the figure legends.

Synaptic density. Images were captured with a $100\times$ objective (NA = 1.49) at a resolution of 1024×1024 pixels. Z-series images were collected in 0.33- μ m steps, and 4 Z-sections (resulting in a total thickness of 1μ m) were stacked using ImageJ (NIH) for quantification of synaptic density. Binary images were created for each channel, and the colocalization between presynapses and postsynapses was determined. The number of colocalized puncta was quantified in the field of view. For each mouse, six separate regions were imaged in the middle molecular layer and processed in this manner, and the average value from these regions was considered as N=1. Multiple mice were used for each experiment, with detailed information provided in the figure legends.

Synaptic phagocytosis by microglia. Images were captured with a 60×0 objective (NA = 1.35) at a resolution of 1024×1024 pixels. Z-series images were collected in 0.33- μ m steps, and 10 Z-sections (resulting in a total thickness of 2.97 μ m) were stacked using ImageJ (NIH) for quantification of synaptic phagocytosis by microglia. For each mouse, four separate regions were imaged in the middle molecular layer and

processed in this manner, and the average value from these regions was considered as N=1. Multiple mice were used for each experiment, with detailed information provided in the figure legends.

Synapse engulfment was quantified using a modified protocol based on previous studies 9,44 . Threshold levels for microglial, synaptic, and CD68 immunofluorescent signals were established in ImageJ. Colocalized images of microglia with synapses or CD68 were then generated, and the volumes of microglia and synaptic signals within CD68-labeled lysosomes were quantified in the middle molecular layer. Synapse engulfment by microglia was calculated using the formula: Volume of internalized synaptic puncta (μm^3) / Volume of microglia (μm^3) .

Synaptic phagocytosis by astrocytes. Images were captured with a $100\times$ objective (NA = 1.49) at a resolution of 1024×1024 pixels. Z-series images were collected in $0.33\text{-}\mu\text{m}$ steps, and 45-60 Z-sections (resulting in a total thickness of $14.52\text{-}19.47\,\mu\text{m}$) were stacked using ImageJ (NIH) for quantification of synaptic phagocytosis by astrocytes. For each mouse, four separate regions were imaged in the middle molecular layer and processed in this manner, and the average value from these regions was considered as N=1. Multiple mice were used for each experiment, with detailed information provided in the figure legends.

Threshold levels for astrocytic, synaptic, and LAMP1 immunofluorescent signals were established in ImageJ. Colocalized images of astrocytes with synapses or LAMP1 were then generated, and the volumes of astrocytes and synaptic signals within LAMP1-labeled lysosomes were quantified in the middle molecular layer. Synapse engulfment by astrocytes was calculated using the formula: Volume of internalized synaptic puncta (µm³) / Volume of astrocyte (µm³).

Microglia synapse touch analysis. Images were captured with a $100\times$ objective (NA = 1.49) at a resolution of 1024×1024 pixels. Z-series images were collected in 0.33- μ m steps, and 10 Z-sections (resulting in a total thickness of $2.97\,\mu$ m) were stacked using ImageJ (NIH) for microglia synapse touch analysis (Supplementary Fig. 13). For each of the 20 microglia from four FS-experiencing mice analyzed, 29-143 VGAT-positive inhibitory synapses (including both touched and untouched synapses) within a single microglial region (defined as the smallest circle encompassing all processes extending in the xy direction) were quantified. The mean intensities of cleaved caspase-3 in both touched and untouched inhibitory presynapses were measured and compared between the two groups.

Establishment and validation of mSCAT3

Molecular cloning. For pcDNA3.1-mSCAT3DEVD/DEVG, A206K (GCC to AAG) mutations for both ECFP and Venus were introduced via PCRbased site-directed mutagenesis from pcDNA3.1-SCAT3 (16) and ligated into a BamHI/HindIII-digested pcDNA3.1-SCAT3 vector using In-Fusion. For pcDNA3.1-Synaptophysin-SCAT3^{DEVD/DEVG} and pcDNA3.1-Synaptophysin-mSCAT3^{DEVD/DEVG}, the coding sequences of Synaptophysin were PCR-amplified from pAAV-hSyn-Synaptophysin-mCherry. The coding sequences of SCAT3^{DEVD/DEVG} and mSCAT3^{DEVD/DEVG} were PCR-amplified from pcDNA3.1-SCAT3^{DEVD/DEVG} and pcDNA3.1mSCAT3^{DEVD/DEVG}. Then, both fragments were ligated into a BamHI/ HindIII-digested pcDNA3.1-SCAT3 vector using In-Fusion. For pAAVhSyn-Synaptophysin-mSCAT3^{DEVD/DEVG}, the coding sequences of mSCAT3^{DEVD/DEVG} were PCR-amplified from pcDNA3.1-mSCAT3^{DEVD/DEVG} and ligated into a BamHI/HindIII-digested pAAV-hSyn-SynaptophysinmCherry vector using In-Fusion.

Cell culture. HeLa cells were grown at 37 °C in DMEM (high glucose) with L-glutamine, phenol red and sodium pyruvate (Wako, #041-30085) supplemented with 10% (v/v) heat-inactivated FBS (NICHIREI, #175012), 100 U/mL penicillin and 100 µg/mL streptomycin (Wako, #168-23191).

Live imaging. Cells were seeded in four-compartment glass bottom dishes (Greiner, #627870) with DMEM (Wako, #040-30095) supplemented with 1 mM sodium pyruvate (Gibco, #11360-070), 1× GlutaMAX supplement (Gibco, #35050-061), 10% (v/v) heat-inactivated FBS, 100 U/mL penicillin, and 100 µg/mL streptomycin. Cells were transfected with the desired plasmids using PEI-Max (Polysciences, #24765) and incubated for 24 hours. Then, the cells were treated with 50 ng/mL TNF α (Wako, #94948-59-1) and 10 µg/mL cycloheximide (Sigma, #C7698) for apoptosis induction. Time-lapse imaging was conducted using a TCS-SP8 confocal microscope (Leica) at 2-minute intervals. mECFP was excited using a 448 nm laser, and the emissions of mECFP and mVenus (FRET) were determined simultaneously using two Leica HyD detectors (450–500 nm and 510–550 nm, respectively). Images were analyzed and edited using Imagel software.

Western blotting. Cells were seeded in 12-well plates with L-glutamine, phenol red and sodium pyruvate supplemented with 10% (v/v) heatinactivated FBS, 100 U/mL penicillin, and 100 µg/mL streptomycin. Cells were transfected with the desired plasmids using PEI-Max (Polysciences, #24765) and incubated for 24 hours. To induce apoptosis. cells were treated with 50 ng/mL TNF α (Wako, #94948-59-1) and 10 μ g/ mL cycloheximide (Sigma, #C7698) for 6 hours. Cells were washed with ice-cold PBS twice and directly lysed using radioimmunoprecipitation assay (RIPA) buffer (50 mM Tris-HCl, pH 8.0, 150 mM sodium chloride, 0.5 w/v% sodium deoxycholate, 0.1% w/v sodium dodecyl sulfate and 1.0% w/v NP-40) supplemented with cOmplete ULTRA EDTA-free protease inhibitor cocktail (Roche, #05892953001). Samples were centrifuged at 20,000 × g and 4 °C for 10 minutes. The supernatants were collected and snap-frozen in liquid nitrogen. Protein concentrations were determined using the BCA assay (Wako, #297-73101) following the manufacturer's protocol. The samples were mixed with 6× Laemmli buffer and boiled at 95 °C for 5 minutes. Samples were separated using SDS-PAGE and transferred onto Immobilon-P PVDF membranes (Millipore, #IPVH00010) for immunoblotting. Membranes were blocked with 4% skim milk diluted in 1× Tris buffered saline with Tween (TBST), Immunoblotting was performed using the antibodies mentioned below, which were diluted with 4% skim milk. Signals were visualized using Immobilon Western Chemiluminescent HRP Substrate (Millipore, #WBKLS0500) and FUSION SOLO. 7S. EDGE (Vilber-Lourmat). Contrast and brightness adjustments were uniformly applied using ImageJ software.

The primary antibodies used were mouse anti-myc monoclonal antibody (1:5,000, Invitrogen, #46-0603) and rabbit anti-Caspase-3 polyclonal antibody (1:10,000, Abcam, #ab184787). Mouse anti-alpha tubulin (DM1A) monoclonal antibody (1:10,000, Sigma, #T9026) was used as a loading control. The secondary antibodies used were HRP-conjugated goat anti-rabbit IgG antibody (1:5,000, Cell Signaling Technology, #7074S) and HRP-conjugated goat anti-mouse IgG antibody (1:5,000, Promega, #W402B).

Fluorescent labeling of C1qA

C1qA-647 was made in-house using recombinant mouse C1qA (Abcam, #ab91203) and an Alexa Fluor™ 647 Antibody Labeling Kit (Thermo Fisher, #A20173) following the manufacturer's instructions.

Optogenetic activation of caspase-9

Light stimulation of CRY2-casp9 was performed using a SpinSR10 equipped with an LED light (Prizmatix) and a pattern illumination system (Polygon 1000, OPTO-LINE). Samples were observed under a $60\times$ objective (NA = 1.5), and 460 nm light at 200 μ W was delivered to a single presynapse detected by synaptophysin-mCherry for 15 minutes.

FS induction and monitoring

Complex FSs were induced by exposing P11 mice to hyperthermia. Hyperthermic conditions were maintained via a regulated stream of

moderately heated air. The core temperature of the mice was raised gradually and measured as the rectal temperature every 2 minutes. A rectal temperature between 39.5 and 43 °C was maintained for 30 minutes. The definition of clonic seizures was behavioral seizures with hindlimb clonus and falling. Drugs were administered 15 minutes before the induction of hyperthermia.

Intrahippocampal injection

Surgery was performed before the induction of FSs. Mice were anesthetized with isoflurane, and lidocaine was subcutaneously injected into the head area before the incision for local anesthesia. The mouse head was fixed in place using a fixation device made by cutting the tip of a 1.5 mL tube, according to a previous protocol⁴⁵. After an incision was made on the head, the heights of the bregma and lambda were aligned by adjusting the fixation device. A 26 G needle (TERUMO, #NN-2613S) was used to make a hole in the skull at the administration site. To target the dentate gyrus of the hippocampus (DP = +1.5 mm, AP = -1.5 mm, ML = 1.5 mm), 500 nL of Z-DEVD-FMK (400 μM in PBS, Adooq, #A13503) or 500 nL of DMSO diluted in PBS to the same concentration as the control was injected into both sides of the hippocampus at a rate of 200 nL/ minute using a syringe pump (KD Scientific Inc., #30-0034). To avoid aggregation of PSVue, 500 nL of PSVue® 643 (1 mM in water, Molecular Targeting Technologies, #P-1006) was injected into both sides of the hipocampus after Z-DEVD-FMK injection. Finally, the head was sutured, and the mice were allowed to recover on a heat pad for 15 minutes.

Quantitative real-time PCR (RT-qPCR) in vivo

After the FS experiments, whole hippocampi were dissected with scissors. Total RNA was extracted using an RNeasy Plus Mini Kit (Qiagen). The RNA samples were reverse-transcribed into cDNA using a SuperScript VILO cDNA Synthesis Kit (Invitrogen), and the cDNA was subjected to RT–qPCR. Quantitative RT–qPCR was conducted in a 20 μL reaction containing LightCycler TaqMan Master Mix (Roche) and using a LightCycler II (Roche). The expression levels of CD11b were normalized to those of β-actin. Primer sets were designed by Universal Probe Library (Roche): CD11b, 5′-tgtccctggctgtttctactg-3′ and 5′-attctccttgcagttttggtg-3′, TaqMan probe #3; β-actin, 5′- ctaaggccaaccgtgaaaag-3′ and 5′- accagaggcatacagggaca-3′, TaqMan probe #64.

Kainic acid seizure induction and monitoring

Three days after the induction of FSs, kainic acid (3 mg/kg, Tocris, #7065) was intraperitoneally administered to the mice, and convulsive seizures were observed over time. We have established our own seizure scores based on careful observation of mouse behavior and our previous study⁴⁶: (1) immobility; (2) repetitive scratching, gustatory movement; (3) rigid posture, pivoting, limb clonus; (4) rearing, falling; (5) clonic seizure, jumping, running; (6) tonic-clonic seizure, jumping (interval); and (7) death.

Statistical analysis

Statistical analyses were performed using GraphPad Prism statistical software. For all comparisons, groups were assessed for normal distribution. If the data were normally distributed, two-tailed unpaired t tests were used for comparing differences between two groups. If the data were not normally distributed, two-tailed Mann–Whitney U tests for comparing differences between two groups. For samples with multiple groups, one-way or two-way analysis of variance (ANOVA) with post hoc tests was performed. If the data were not normally distributed, one-way ANOVA on ranks with post hoc tests was used. No data points were excluded from the analysis. Data are presented as the mean \pm standard deviation (SD). Data collection and analysis were

blindly performed in all experiments. Data for each experiment were collected and processed randomly, and animals were randomly assigned to various experimental groups.

Reporting summary

Further information on research design is available in the Nature Portfolio Reporting Summary linked to this article.

Data availability

All data necessary to evaluate the conclusions in this paper are included within the main text and Supplementary Materials. Given the large volume of image data generated in this study, we have included key representative images within the figures and Supplementary Information. Additional image data can be made available upon request due to storage limitations and practical considerations. Source data are provided with this paper.

References

- Nguyen, H. et al. BAF (mSWI/SNF) complex regulates mediolateral cortical patterning in the developing forebrain. Front Cell Dev Biol 10, 1011109 (2022).
- Yamaguchi, Y. & Miura, M. Programmed cell death in neurodevelopment. Dev Cell 32, 478–490 (2015).
- Campbell, D. S. & Okamoto, H. Local caspase activation interacts with Slit-Robo signaling to restrict axonal arborization. *J Cell Biol* 203, 657–672 (2013).
- Cusack, C. L., Swahari, V., Hampton Henley, W., Michael Ramsey, J. & Deshmukh, M. Distinct pathways mediate axon degeneration during apoptosis and axon-specific pruning. *Nat Commun* 4, 1876 (2013).
- Li, Z. et al. Caspase-3 activation via mitochondria is required for long-term depression and AMPA receptor internalization. *Cell* 141, 859–871 (2010).
- Ertürk, A., Wang, Y. & Sheng, M. Local pruning of dendrites and spines by caspase-3-dependent and proteasome-limited mechanisms. J Neurosci 34, 1672–1688 (2014).
- Dehkordi, M. H., Munn, R. G. K. & Fearnhead, H. O. Non-Canonical Roles of Apoptotic Caspases in the Nervous System. Front Cell Dev Biol 10, 840023 (2022).
- Huesmann, G. R. & Clayton, D. F. Dynamic role of postsynaptic caspase-3 and BIRC4 in zebra finch song-response habituation. *Neuron* 52, 1061–1072 (2006).
- Schafer, D. P. et al. Microglia sculpt postnatal neural circuits in an activity and complement-dependent manner. *Neuron* 74, 691–705 (2012).
- Paolicelli, R. C. et al. Synaptic pruning by microglia is necessary for normal brain development. Science 333, 1456–1458 (2011).
- Györffy, B. A. et al. Local apoptotic-like mechanisms underlie complement-mediated synaptic pruning. *Proc Natl Acad Sci USA* 115, 6303–6308 (2018).
- Vasek, M. J. et al. Local translation in microglial processes is required for efficient phagocytosis. *Nat Neurosci* 26, 1185–1195 (2023).
- Nanou, E. & Catterall, W. A. Calcium Channels, Synaptic Plasticity, and Neuropsychiatric Disease. Neuron 98, 466–481 (2018).
- Ow, Y. P., Green, D. R., Hao, Z. & Mak, T. W. Cytochrome c: functions beyond respiration. Nat Rev Mol Cell Biol 9, 532–542 (2008).
- Vaccaro, V., Devine, M. J., Higgs, N. F. & Kittler, J. T. Miro1dependent mitochondrial positioning drives the rescaling of presynaptic Ca²⁺ signals during homeostatic plasticity. *EMBO Rep.* 18, 231–240 (2017).
- Takemoto, K., Nagai, T., Miyawaki, A. & Miura, M. Spatio-temporal activation of caspase revealed by indicator that is insensitive to environmental effects. J Cell Biol 160, 235–243 (2003).

- 17. Stevens, B. et al. The classical complement cascade mediates CNS synapse elimination. *Cell* **131**, 1164–1178 (2007).
- Chu, Y. et al. Enhanced synaptic connectivity and epilepsy in C1q knockout mice. Proc Natl Acad Sci USA 107, 7975–7980 (2010).
- Lui, H. et al. Progranulin Deficiency Promotes Circuit-Specific Synaptic Pruning by Microglia via Complement Activation. Cell 165, 921–935 (2016).
- Hong, S. et al. Complement and microglia mediate early synapse loss in Alzheimer mouse models. Science 352, 712–716 (2016).
- Mandal, D., Moitra, P. K., Saha, S. & Basu, J. Caspase 3 regulates phosphatidylserine externalization and phagocytosis of oxidatively stressed erythrocytes. FEBS Lett 513, 184–188 (2002).
- Païdassi, H. et al. C1q binds phosphatidylserine and likely acts as a multiligand-bridging molecule in apoptotic cell recognition. J Immunol 180, 2329–2338 (2008).
- Tichy, A. M., Gerrard, E. J., Legrand, J. M. D., Hobbs, R. M. & Janovjak, H. Engineering Strategy and Vector Library for the Rapid Generation of Modular Light-Controlled Protein-Protein Interactions. *J Mol Biol* 431, 3046–3055 (2019).
- D'Amelio, M. et al. Caspase-3 triggers early synaptic dysfunction in a mouse model of Alzheimer's disease. Nat Neurosci 14, 69–76 (2011).
- Kasahara, Y., Igata, H., Sasaki, T., Ikegaya, Y. & Koyama, R. The Pharmacological Assessment of GABA_A Receptor Activation in Experimental Febrile Seizures in Mice. eNeuro 6, e0429-18 (2019).
- Jamali, S. et al. Functional variant in complement C3 gene promoter and genetic susceptibility to temporal lobe epilepsy and febrile seizures. PLoS One 5, e12740 (2010).
- Favuzzi, E. et al. GABA-receptive microglia selectively sculpt developing inhibitory circuits. Cell 184, 4048–4063.e4032 (2021).
- Sierra, A. et al. Microglia shape adult hippocampal neurogenesis through apoptosis-coupled phagocytosis. *Cell Stem Cell* 7, 483–495 (2010).
- Cunningham, C. L., Martínez-Cerdeño, V. & Noctor, S. C. Microglia regulate the number of neural precursor cells in the developing cerebral cortex. *J Neurosci* 33, 4216–4233 (2013).
- 30. Mazaheri, F. et al. Distinct roles for BAI1 and TIM-4 in the engulfment of dying neurons by microglia. *Nat Commun* **5**, 4046 (2014).
- Kamei, R. & Okabe, S. In vivo imaging of the phagocytic dynamics underlying efficient clearance of adult-born hippocampal granule cells by ramified microglia. *Glia* 71, 2005–2023 (2023).
- Orrenius, S., Zhivotovsky, B. & Nicotera, P. Regulation of cell death: the calcium-apoptosis link. Nat Rev Mol Cell Biol 4, 552–565 (2003).
- Xu, J. H., Long, L., Tang, Y. C., Hu, H. T. & Tang, F. R. Ca(v)1.2, Ca(v) 1.3, and Ca(v)2.1 in the mouse hippocampus during and after pilocarpine-induced status epilepticus. *Hippocampus* 17, 235–251 (2007).
- Guo, J. et al. BDNF pro-peptide regulates dendritic spines via caspase-3. Cell Death Dis 7, e2264 (2016).
- Pekkurnaz, G. & Wang, X. Mitochondrial heterogeneity and homeostasis through the lens of a neuron. Nat Metab 4, 802–812 (2022).
- Hollville, E. & Deshmukh, M. Physiological functions of nonapoptotic caspase activity in the nervous system. Semin Cell Dev Biol 82, 127–136 (2018).
- Martin, M., Leffler, J. & Blom, A. M. Annexin A2 and A5 serve as new ligands for C1q on apoptotic cells. *J Biol Chem* 287, 33733–33744 (2012).
- Peng, Z. & Houser, C. R. Temporal patterns of fos expression in the dentate gyrus after spontaneous seizures in a mouse model of temporal lobe epilepsy. J Neurosci 25, 7210–7220 (2005).
- Muldoon, S. F. et al. GABAergic inhibition shapes interictal dynamics in awake epileptic mice. *Brain* 138, 2875–2890 (2015).

- Vinet, J. & Sík, A. Expression pattern of voltage-dependent calcium channel subunits in hippocampal inhibitory neurons in mice. *Neuroscience* 143, 189–212 (2006).
- 41. Santuy, A. et al. A Quantitative Study on the Distribution of Mitochondria in the Neuropil of the Juvenile Rat Somatosensory Cortex. *Cereb Cortex* **28**, 3673–3684 (2018).
- 42. Zhou, Z. et al. Astrocytic cAMP modulates memory via synaptic plasticity. *Proc. Natl Acad. Sci. USA* **118**, e2016584118 (2021).
- Aurnhammer, C. et al. Universal real-time PCR for the detection and quantification of adeno-associated virus serotype 2-derived inverted terminal repeat sequences. *Hum Gene Ther Methods* 23, 18–28 (2012).
- 44. Andoh, M. et al. Exercise Reverses Behavioral and Synaptic Abnormalities after Maternal Inflammation. *Cell Rep.* **27**, 2817–2825.e2815 (2019).
- 45. Chen, S. Y., Kuo, H. Y. & Liu, F. C. Stereotaxic Surgery for Genetic Manipulation in Striatal Cells of Neonatal Mouse Brains. *J. Vis. Exp.* **137**, e57270 (2018).
- Koyama, R. et al. GABAergic excitation after febrile seizures induces ectopic granule cells and adult epilepsy. *Nat Med.* 18, 1271–1278 (2012).

Acknowledgements

Grant-in-Aid for Transformative Research Areas (A) "Glia decoding" (20H05897) from Japan Society for the Promotion of Science (R.K.) Adopting Sustainable Partnerships for Innovative Research Ecosystem (JP24jf0126004s0402) from Japan Agency for Medical Research and Development (R.K.). Exploratory Research for Advanced Technology (JPMJER1801) from Japan Science and Technology Agency (Y.I.). Grants (21H04774, 23H04766, 24H00567) from the Japan Society for the Promotion of Science (MM).

Author contributions

M.A. played a primary role in conceiving this study, developing experimental methods, and performing experiments. All authors contributed to data analyses. M.A. and R.K. designed the project. N.S., Y.T., and M.M. developed the probes to detect caspase activity and analyzed its properties. T.A. performed the in vivo DEVD injections. Y.K. conducted the behavioral seizure scoring. H.T. performed qPCR analysis. M.M., Y.I. and R.K. acquired funding. M.A. and R.K. wrote the manuscript, which was edited by all of the authors. R.K. managed the project.

Competing interests

The authors declare no competing interests.

Additional information

Supplementary information The online version contains supplementary material available at

https://doi.org/10.1038/s41467-025-56342-7.

Correspondence and requests for materials should be addressed to Ryuta Koyama.

Peer review information *Nature Communications* thanks Shigeo Okabe, Ilse Smolders and the other, anonymous, reviewer(s) for their contribution to the peer review of this work. A peer review file is available.

Reprints and permissions information is available at http://www.nature.com/reprints

Publisher's note Springer Nature remains neutral with regard to jurisdictional claims in published maps and institutional affiliations.

Open Access This article is licensed under a Creative Commons Attribution-NonCommercial-NoDerivatives 4.0 International License, which permits any non-commercial use, sharing, distribution and reproduction in any medium or format, as long as you give appropriate credit to the original author(s) and the source, provide a link to the Creative Commons licence, and indicate if you modified the licensed material. You do not have permission under this licence to share adapted material derived from this article or parts of it. The images or other third party material in this article are included in the article's Creative Commons licence, unless indicated otherwise in a credit line to the material. If material is not included in the article's Creative Commons licence and your intended use is not permitted by statutory regulation or exceeds the permitted use, you will need to obtain permission directly from the copyright holder. To view a copy of this licence, visit http://creativecommons.org/licenses/by-nc-nd/4.0/.

© The Author(s) 2025